JCI insight

Live Cell Imaging of Human Liver Fibrosis using Hepatic Micro-Organoids

Yuan Guan, … , Annika Enejder, Gary Peltz

Research In-Press Preview **Hepatology**

Due to the limitations of available *in vitro* systems and animal models, we lack a detailed understanding of the pathogenetic mechanisms and have minimal treatment options for liver fibrosis. Therefore, we engineered a live cell imaging system that assesses fibrosis in a human multi-lineage hepatic organoid in a microwell (i.e., microHOs). Transcriptomic analysis revealed that TGFβ1 converted mesenchymal cells in microHOs into myofibroblast-like cells resembling those in fibrotic human liver tissue. When pro-fibrotic intracellular signaling pathways were examined, the anti-fibrotic effect of receptor-specific tyrosine kinase inhibitors was limited to the fibrosis induced by the corresponding growth factor, which indicates their anti-fibrotic efficacy would be limited to fibrotic diseases solely mediated by that growth factor. Based upon transcriptomic and transcription factor activation analyses in microHOs, GSK3β and p38 MAPK inhibitors were identified as potential new broad-spectrum therapies for liver fibrosis. Other new therapies could subsequently be identified using the microHO system.

Find the latest version:

https://jci.me/187099/pdf

Live Cell Imaging of Human Liver Fibrosis using Hepatic Micro-Organoids

Yuan Guan, Zhuoqing Fang, Angelina Hu, Sarah Roberts, Meiyue Wang, Wenlong Ren, Patrik K. Johansson[1], Sarah C. Heilshorn[1], Annika Enejder[1] and Gary Peltz[*]

Department of Anesthesia, Pain and Perioperative Medicine, Stanford University School of Medicine, Stanford CA, 94305; and [1]Department of Materials Science and Engineering, Stanford University, Stanford CA, 94305

Key Words: Liver Fibrosis, Hepatic Organoids, Anti-Fibrotic Drug Screening

Word Count: 9739 (including 2569 words in figure legends) Figures: 8

*Address Correspondence to: gpeltz@stanford.edu 300 Pasteur Dr. Room L232 Stanford, CA 94305.

Abstract

Due to the limitations of available *in vitro* systems and animal models, we lack a detailed understanding of the pathogenetic mechanisms and have minimal treatment options for liver fibrosis. Therefore, we engineered a live cell imaging system that assessed fibrosis in a human multi-lineage hepatic organoid in a microwell (i.e., microHOs). Transcriptomic analysis revealed that TGFB converted mesenchymal cells in microHOs into myofibroblast-like cells resembling those in fibrotic human liver tissue. When pro-fibrotic intracellular signaling pathways were examined, the anti-fibrotic effect of receptor-specific tyrosine kinase inhibitors was limited to the fibrosis induced by the corresponding growth factor, which indicates their anti-fibrotic efficacy would be limited to fibrotic diseases solely mediated by that growth factor. Based upon transcriptomic and transcription factor activation analyses in microHOs, GSK3β and p38 MAPK inhibitors were identified as potential new broad-spectrum therapies for liver fibrosis. Other new therapies could subsequently be identified using the microHO system.

Word count: 150

Abbreviations: ARPKD, Autosomal Recessive Polycystic Kidney Disease; ECM, extra-cellular matrix; GSEA, gene set enrichment analysis; HCS, high content screening; HO, hepatic organoid; HCC, hepatocellular carcinoma; HSC, hepatic stellate cells; iPSC, induced pluripotent stem cells; MAPK, Mitogen Activated Protein Kinase; NASH, non-alcoholic steatohepatitis; SHG, Second Harmonic Generation; TF, transcription factor.

Liver fibrosis is a pathological condition caused by the accumulation of extracellular matrix (**ECM**) that develops in response to chronic liver injury (1). It results from an interaction between parenchymal and nonparenchymal liver cells and involves endogenous and liver infiltrating immune cells (2-4). The key non-parenchymal cell is the myofibroblast, which is generated when a fibrogenic stimulus induced by liver injury causes hepatic stellate cells (**HSC**) to transdifferentiate into myofibroblasts that produce fibril-forming collagens and other ECM components (4-8). Before organoid methodology was available, *in vitro* models often did not have the spectrum of cell types that mediate fibrogenesis, which limited our ability to explore fibrogenic mechanisms. Commonly used rodent models require an injury inducing agent (carbon tetrachloride, bile duct ligation, or dietary modulation); are very time consuming and expensive to run; and any conclusions drawn from them are limited by concerns about their fidelity with the processes mediating the commonly occurring forms of human liver fibrosis (9). However, the pathogenesis of liver fibrosis can best be studied using a multi-lineage human hepatic organoid (**HO**) that has the cellular components and the geometry of hepatic lobules, which enables the effect that biochemical signals have on fibrosis to be quantitatively characterized. We previously developed an *in vitro* model system that differentiates human induced pluripotent stem cells (**iPSCs**) into a multi-lineage HO that has hepatocytes, cholangiocytes, HSCs, and cells of other lineages (fibroblasts, macrophages, and endothelial cells); and other structures found in the liver lobule are formed in these HOs (10, 11). HOs engineered to express a causative mutation for Autosomal Recessive Polycystic Kidney Disease (**ARPKD**) developed an extensive fibrosis (11) characterized by a marked increase in thick collagen fiber formation, which resembled that in liver tissue obtained from ARPKD patients. The myofibroblasts in ARPKD organoids resembled those in the livers of patients with viral-induced cirrhosis or advanced non-alcoholic steatohepatitis (**NASH**) (11). Here, we engineered a live cell imaging system for identification of the collagen producing cells in hepatic organoids that was adapted for use in a microwell-based platform. This system was used to characterize the signals driving liver fibrosis at the whole

3

organoid, single cell, and molecular levels. Moreover, when the interaction between the intracellular signaling pathways activated by two pro-fibrotic factors were characterized, two potential new approaches for treating liver fibrosis were identified.

Results

A live cell imaging system for hepatic fibrosis. Collagen is a triple helical protein that is composed of two COL1A1 (α1) and one COL1A2 (α2) chains, and increased collagen synthesis by activated myofibroblasts is a major contributor to liver fibrosis (12). To characterize fibrogenic mechanisms, we developed a live cell imaging system, which enabled collagen producing cells in HOs to be identified and quantitatively analyzed. A CRISPR-assisted insertion tagging system (CRISPaint) (13) was used to insert a Clover expression cassette (**COL1A1-P2A Clover**) at the COOH terminus of the endogenous *COL1A1* gene in a control iPSC line. Since the insert has a self-cleaving P2A peptide, *COL1A1* mRNA expressing cells in HOs produced from *COL1A1*-P2A Clover iPSCs were labelled with a fluorescent intracellular protein (**Fig. 1A-B**). The Clover$^+$ cell population increased in HO cultures at the hepatoblast stage (day 9) (**Fig. 1C-D**). Immunostaining and flow cytometry revealed that Clover$^+$ cells: were markedly increased in day 21 HOs that were treated with TGFB or PDGFB on day 13; co-expressed PDGFRβ and COL1A1; were present throughout the organoid; and were distinct from hepatocytes or cholangiocytes (**Figs. 1E-G, S1**). The flow cytometry results confirm that Clover fluorescence is cell based (**Figs. 1D**, **1G**). The pro-fibrotic effect of TGFB and PDGFB was consistent with the temporal pattern of expression of mRNAs encoding their receptors (*PDGFRA, PDGFRB, TGFBR1, TGFBR2, TGFBR3, BMPR1B*) and intracellular signaling proteins (STATs, SMADs), which were expressed at the hepatoblast stage (day 9) (i.e., prior to exposure to PDGFB or TGFB on day 13) and in mature HOs (**Fig. S2**). Clover protein was expressed at an extremely

low level in iPSC and its expression was slightly increased in hepatoblasts, but its was more abundantly expressed in control, TGFB- and PDGFB-treated mature HOs (**Fig. 1H**).

The spatial distribution and morphology of the collagen fibers in HOs were examined using Second Harmonic Generation (**SHG**) microscopy (14, 15), which has previously been used to quantitatively analyze liver fibrosis in human patients (16, 17) and to monitor fibrosis in ARPKD HOs (11). Of importance, SHG measures thick collagen fiber formation; which is a complex biochemical pathway that requires the coordinated activity of multiple liver enzymes that include proteases and other post-translational processing enzymes that act on collagen, and subsequently the activity of lysyl hydroxylases and lysyl oxidases to generate thick collagen fibers. (18). SHG images revealed that control HOs had sporadic networks of cross-linked collagen fibers surrounding the cells in some isolated regions, while the TGFB or PDGFB-treated organoids had more extensive networks of thick collagen fibers throughout the entire HO. A quantitative comparison indicated that TGFB ($p < 0.05$) or PDGFB ($p < 0.01$) exposure induced statistically significant increases in total collagen abundance and in the abundance of thick collagen fibers (i.e., > 3 um diameter) formed in HOs ($p<0.01$) (**Fig. 1I**). The SHG and immunostaining results indicate that PDGFB or TGFB increases the numbers of collagen synthesizing cells and the amount of thick collagen fibers formed in HOs.

*A high content screening system (**HCS**) for serially monitoring the effect of biochemical signals on liver fibrosis*. Culture conditions were modified to enable HOs to reproducibly grow to a standard size in microwells, which we refer to as '*microHOs*' (**Fig. 2A-B**). Trichrome staining confirmed that TGFB or PDGFB induced a large increase in collagen in microHOs (**Fig. 2C**). The TGFB effect on thick collagen fiber formation was confirmed by 4-hydroxyproline (4OH-Pro) measurements: 4OH-Pro was absent in iPSC; it increased in day 9 hepatoblasts and in day 21 control HOs; but was significantly increased after PDGFB or TGFB exposure ($p<0.001$ vs

control) (**Fig. 2D**). HCS was performed using a confocal fluorescence microplate imager with an automated program that we developed for analyzing multiple Z-stacked confocal images. The TGFB concentration used to induce fibrosis was determined to be 50 ng/ml (**Fig. S3**). TGFB addition on day 13 induced a sustained increase in COL1A1$^+$ cells in microHOs that was blocked by co-administration of TGFBR1 tyrosine kinase inhibitors (10 uM SB431542 (19, 20) or A83-01 (21)) (**Fig. 2E-F**). PDGFB addition on day 13 also increased the number of COL1A1$^+$ cells in microHOs, which was blocked by addition of a PDGFRβ tyrosine kinase inhibitor (10 uM Imatinib (22) (**Fig. 2G-H**).

The microHO system was also used to examine the effect of other agents - five cytokines (IL-4 (23), IL-6 (24), IL-13, IL-33 (25, 26), TNFα (27)) and three growth factors (IGF1 (28), VEGF (29), CCL3 (30)) - that had been directly or indirectly implicated in the pathogenesis liver fibrosis. None of these agents induced fibrosis in microHOs (**Fig. S4**). Analysis of the temporal pattern of receptor expression in differentiating HO cultures using previously obtained transcriptomic data (11) revealed that the mRNAs encoding the IGF-1 (*IGF1R*), IL13 (*IL13RA1*), and VEGF (*VEGFR-1 (FLT1)*; *VEGFR-2 (KDR)*) receptors were expressed in day 9 hepatoblasts and in mature (day 21) organoids. In contrast, the mRNAs encoding the receptors for IL33 (*IL1RL1 or ST2*), IL4 (*IL4R*), or for the common gamma chain that is used for intra-cellular signaling by multiple cytokine receptors (*IL2RG*) were not expressed in day 9 hepatoblasts (**Fig. S5A**). Of note, the mRNAs encoding most of these receptors are abundantly expressed in mature HOs (**Fig. S5B**). Hence, the lack of a profibrotic effect of IGF-1 and VEGF is not due to the absence of receptor expression when microHOs were exposed to these agents. However, the lack of a profibrotic effect of IL-4 and IL-13 could result from the absence of functional receptors on day 9, which is just before the time of exposure to those cytokines. Since the hedgehog signaling pathway activation increases *COL1A1* mRNA expression in

myofibroblasts (31) and promotes myofibroblast accumulation and liver fibrosis (32), we examined whether a hedgehog pathway activator would induce fibrosis in microHOs. Smoothened (**SMO**) is a seven transmembrane protein (33, 34) that accumulates in the primary cilium, and transduces a Hedgehog pathway signal intracellularly. However, addition of a SMO agonist (SAG), which activates Hedgehog signaling (35), did not induce fibrosis in microHO cultures (**Fig. S4**).

The Clover$^+$ population represents mesenchymal cells and myofibroblasts. To characterize the pro-fibrotic effects of PDGFB and TGFB, scRNA-seq data was generated from day 21 control (22,211 cells), TGFB-treated (17,554 cells) or PDGFB-treated (18,013 cells) microHOs. Eleven cell clusters were identified by analysis of this scRNA-seq dataset (**Fig. 3A, Table S3**). The differentially expressed genes and the gene ontology biological process annotations (GO) for each cluster were analyzed to identify the cell type represented by each cluster (**Fig. 3B, S6** and **Table S4**). Based upon expression of canonical mRNAs and by the level of concordance between their transcriptomes with the cell types in human liver, the microHOs have cholangiocyte (Cho1-3), hepatocyte (Hep), mesenchymal cell (Mes1-4) and myofibroblast (MyoF_T1-2, MyoF_P) clusters. Also, *COL1A1* and *Clover* mRNAs have an identical pattern of expression in the microHOs: both mRNAs are expressed in myofibroblasts and mesenchymal cells. In contrast, an epithelial mRNA (*EPCAM)* that is a hepatoblast and cholangiocyte marker was not expressed in the *Clover* mRNA$^+$ cells (**Fig. 3C-D).** Many mRNAs found in cholangiocytes (*KRT19*, *KRT7* and *CFTR)* or in hepatocytes and cholangiocytes (*HNF4A, AFP, CDH1, ALDHA1, APOB, FGB*) were also not expressed in the *Clover* mRNA$^+$ cells in the microHOs (**Fig. S7**). Myofibroblast marker mRNA (*ACTA2, PDGFRA, FAP*) expression was very low in control microHOs, but were predominantly expressed in the myofibroblast (MyoF_T1/2, MyoF_P) clusters in PDGFB- or TGFB-treated microHOs (**Fig. S8**). Consistent with the profile of *FAP* mRNA expression in microHOs (**Fig. S8**), FAP is absent in most tissues under basal

conditions but is highly expressed on activated myofibroblasts (36, 37). FAP is a well-established marker for activated fibroblasts (38) and its serine protease activity promotes liver fibrosis by activating HSC and promoting macrophage infiltration after liver injury (39).

Changes in mesenchymal and epithelial cell clusters in fibrotic microHOs. To systematically examine the changes in the cell types in PDGFB- or TGFB-treated microHOs (vs NC), ANOVA and 'sccomp' (a statistical model using a constrained Beta-binomial distribution (40)) were used to statistically analyze the changes in cell type proportions. The cells in PDGFB- or TGFB-treated microHOs were reproducibly different from those in control microHOs (**Fig. 4A-B, Fig. S9**). One myofibroblast cluster (MyoF_T1) was far more abundant in TGFB-treated microHOs than in control or PDGFB-treated microHOs (37.5% of total vs <2%), while another myofibroblast cluster (MyoF_P) was more abundant in PDGFB-treated microHOs than in control or TGFB-treated microHOs (20% of total vs <2%). The abundance of a mesenchymal cluster (Mes2) was markedly decreased in TGFB or PDGFB-treated microHOs (25% vs <5%) (**Fig. 4C, Table S3**). A one-way ANOVA comparing the different types of cells in each of 5-independent biological replicates analyzed by scRNA-Seq indicated that MyoF_T1 ($p<0.015$) and MyoF_P ($p<0.05$) abundances were significantly increased, while Mes2 abundance was decreased ($p=0.004$) in TGFB- or PDGFB-treated microHOs. The 'sccomp' analysis indicated that the Cho1-2 clusters were significantly decreased, while Cho3 was significantly increased in TGFB-treated microHOs (**Table S5, Fig. S10**).

To better understand the TGFB effect on the mesenchymal and epithelial cell clusters, their differentiation state and other properties were characterized using three different computational methods for analysis of scRNA-Seq data. (i) RNA velocity (41), which assessed the differentiation state of the cell clusters, indicated that MyoF_T1 was the most highly differentiated cluster (**Fig. 4D**). (ii) Cell cycle analysis indicated that TGFB-treated microHOs

8

had the highest percentage of G1 phase cells, which indicates that the cells were less proliferative. At the cluster level, MyoF-T1 and Cho3 had the highest percentage of cells in G1 and the lowest percentage of G2/M and S phase cells, which indicates that those clusters were less proliferative (**Fig. 4E**). (iii) Consistent with the RNA velocity results, Cytotrace2 (42) indicated that MyoF_T1 and MyoF_P were the most differentiated of the mesenchymal cell clusters, whereas Cho3 was the most differentiated epithelial cluster (**Fig. 4F**). These results indicate that MyoF-T1 cells are the most differentiated of the mesenchymal cell populations in fibrotic microHOs, and they have a low level of proliferation after they exit the cell cycle (**Fig. 4E**).

Transcriptomic comparisons with various cell types in control and cirrhotic human liver were performed to further characterize the three clusters whose abundance was significantly altered by TGFB or PDGFB exposure. The results revealed that MyoF_T1 and MyoF_P clusters were most like that of myofibroblasts, whereas Mes2 was most similar to HSC in human liver (**Fig. 4G, Fig. S11, Tables S6-S7**). As described in supplemental note 1, Gene Set Enrichment Analysis (**GSEA**) (43) revealed that the gene expression signature of MyoF_T1 in microHOs resembled those found in fibrotic human liver tissue caused by NASH or hepatocellular carcinoma (**Fig. 4H and S12**, **Table S8**). While the MyoF_P gene signature was positively associated with NASH or HCC-induced liver fibrotic tissue, those GSEA associations did not achieve statistical significance. Also, the pattern of expression of 9 mesenchyme and myofibroblast-specific mRNAs in mesenchymal cells and myofibroblasts in human liver was retained in Mes2 and MyoF_T1 cells in microHOs (**Fig. S13**). Taken together, the transcriptomic results indicate that TGFB or PDGFB exposure converts a population of HSC-like cells into myofibroblast-like cells in microHOs. Since nonparenchymal cells (i.e., the mesenchymal cells in microHOs) and epithelial cell interactions play a key role in liver fibrosis, 'Cellchat' (44) was used to examine cell cluster interactions in fibrotic microHOs and in cirrhotic human liver. It was

noteworthy that the myofibroblasts in cirrhotic liver (or MyoF-T1 in microHOs) and cholangiocytes in cirrhotic liver (or Cho3 in microHOs) had the strongest incoming and outgoing interactions (**Fig. 4I**), which indicates that these cells and pathways could be targeted for pharmacologic intervention. To address the origin of the mesenchymal cells present in microHOs, we examined scRNA-Seq data obtained from iPSC, day 9 hepatoblast and mature HO cultures (**Fig. S14**). Since a distinct subset of cells in the hepatoblast cultures express mRNAs that are mesenchymal cell markers, the mesenchymal cells develop from iPSC at an early differentiation stage.

Identification of drug targets through analysis of transcription factor (TF) activation. TF activity in fibrotic microHOs and in NASH-induced cirrhotic human liver tissue was examined by analysis of scRNA-seq data using the 'decoupleR' method (45). Multiple TFs were activated in fibrotic microHOs and in cirrhotic liver tissue. Among the clusters in microHOs, MyoF_T1 and Cho3 cells exhibited the widest spectrum of TF activation (**Fig. 5A**). Of interest, SMAD4, STAT1 and JUN activity was increased in MyoF_T1 and Cho3 cells after TGFB treatment (versus control, **Fig. 5B-C**). These TFs were also activated cirrhotic NASH liver tissue, and liver myofibroblasts displayed the highest level of activation of these TFs (versus vascular smooth muscle or HSC, **Fig. 5D-E**). PDGFB and TGFB are well established drivers of liver fibrosis (46). TGFRB activation leads to activation of SMAD signaling pathways (47, 48) and PDGFR cross-linking activates the STAT3 pathway (49) (50), and both of these pathways have well-known roles in promoting hepatic fibrosis (50). However, other pathways, which are jointly activated by these profibrotic agents, could provide new targets for anti-fibrotic drugs. Both TGFBR1 (47, 48, 51) and PDGFR (52, 53) activate the p38 Mitogen Activated Protein Kinase (MAPK) and PI3K–Akt–mTOR intracellular signaling pathways, which are also pro-fibrotic (**Fig. 5F**). Of relevance, several TFs in the p38 pathway were activated in MyoF-T1 in fibrotic microHOs (JUN, AP1, FOS) and in the myofibroblasts in cirrhotic human liver (JUNB, FOSB) (**Figs. 5A**, **5D**). Hence,

10

we hypothesized that effective anti-fibrotic agents could be produced by targeting pathways (i.e., p38 or PI3K–Akt–mTOR) that are jointly activated by TGFBRs and PDGFRs.

Pharmacologic characterization of pro-fibrotic signaling pathways. Although the anti-fibrotic effect of the receptor tyrosine kinase inhibitors was growth factor dependent, other signaling pathways jointly activated by the TGFB and PDGFB receptors could also be essential for fibrosis. Therefore, we examined whether co-administration of PI3K-Akt-mTOR (rapamycin) or MAPK pathway (SB202190) inhibitors with PDGFB or TGFB could reduce fibrosis. Co-administration of 10 uM SB202190 – a highly selective p38α and β kinase inhibitor (54) – inhibited both TGFB and PDGFB-induced fibrosis in microHOs (**Fig. 6A-C, Fig. S3C**). Thus, p38 MAPK pathway activity is essential for either PDGFB- or TGFB-driven fibrosis. Rapamycin partially inhibited PDGFB-induced fibrosis but did not inhibit TGFB-induced fibrosis (**Fig. 6D-F**). This result indicates that the downstream part of the PI3K-Akt-mTOR pathway was not essential for TGFB-induced fibrosis, but it could be required for PDGFB-induced fibrosis.

This microHO system could also be used to test the potential anti-fibrotic efficacy of candidate medications for liver fibrosis. For example, nintedanib and pirfenidone are the only two FDA-approved drugs for treatment of pulmonary fibrosis (55). Both inhibit multiple tyrosine kinases and have been shown to reduce lung fibrosis in animal models (1, 56) and in patients with interstitial lung fibrosis (57-61). Although the mechanism for their anti-fibrotic effect is unknown, it has been suggested that they could also be used to treat liver fibrosis (50). However, co-administration of 10 uM pirfenidone or 10 uM nintedanib did not inhibit the TGFB-induced fibrosis in microHOs. While pirfenidone did not inhibit PDGFB-induced fibrosis, nintedanib delayed the onset of PDGFB-induced fibrosis in microHOs (**Fig. 6D-F**). Of note, these concentrations were >10-fold above the nintedanib concentration that inhibited PDGFB-stimulated cellular proliferation (IC$_{50}$ 64 nM) and PDGFR auto-phosphorylation (IC$_{50}$ 22-39 nM)

(62) and of the pirfenidone concentration (1 uM) that inhibited proliferation and *TGFB* mRNA expression (63) in cultured human fibroblasts. The partial inhibitory effect of nintedanib on PDGFB-induced fibrosis is consistent with its inhibition of the PDGFB receptor tyrosine kinase activity (IC_{50} 60 nM) (64).

WNT/β-catenin signaling contributes to the pathogenesis of liver fibrosis (65, 66), which led to the suggestion that it could be targeted by anti-fibrotic therapies (67). Since glycogen synthase kinase 3β (GSK3β)-mediated phosphorylation of β-catenin targets it for ubiquitin-dependent proteasomal degradation, GSK3β inhibitors stabilize β-catenin and promote the transcription of β-catenin target mRNAs (68, 69). Therefore, we examined the effect that co-administration of a Wnt/β-catenin pathway activator (Wnt3a) or of a GSK3β enzyme inhibitor (3 uM CHIR99021), which has been shown to activate the Wnt/β-catenin pathway (70), had on fibrosis in microHOs. Wnt3a co-administration had a minimal effect on the extent of PDGFB- or TGFB-driven fibrosis (**Fig. S4**). The GSK3β inhibitor by itself did not increase COL1A1$^+$ cells in the organoids (**Fig. S4**). However, co-administration of the GSK3β inhibitor with either PDGFB or TGFB blocked fibrosis in microHOs (**Fig. 7, Fig. S3B**). Of importance, cell viability in microHOs was not reduced by addition of TGFB, nor by adding the GSK3β or TGFBR1 inhibitors **(Fig. S15).** Our results indicate that p38 MAPK or GSK3β kinase inhibitors can block liver fibrosis irrespective of whether it is driven by either PDGFB or TGFB.

To determine if the anti-fibrotic effects of the TGFBR1, GSK3β or p38 inhibitors was dependent upon the genetic background of the *COL1A1*-P2A Clover line, we examined their anti-fibrotic effect in microHOs generated from iPSC lines (C1, C2) prepared from two other donors with different genetic backgrounds (10). As visualized by trichrome staining, TGFB induced a marked increase in collagen-rich connective tissue in the C1 and C2 microHOs (p<0.001) that was

markedly inhibited by addition of TGFBR1, GSK3β, or p38 inhibitors (p<0.001) (**Fig. 8**). This result indicates that the anti-fibrotic effect of these drugs was independent of the genetic background of the iPSC used to produce the HO.

Discussion

We demonstrate that microHOs and the live cell imaging system developed here can be used to characterize the biochemical signals and intracellular signaling pathways that drive liver fibrosis and for assessing potential anti-fibrotic therapies. The TGFB and PDGFB-induced fibrosis in microHOs was shown to resemble human fibrotic liver disease based upon the formation of thick collagen fibers (SHG results), and these agents increased collagen crosslinking (4-OHPro measurement) and collagen deposition (trichrome staining) in microHOs. Transcriptomic comparisons demonstrated that the transcriptomes of microHO myofibroblasts resembled the myofibroblasts in fibrotic human liver tissue. Of the agents tested– which included cytokines, growth factors, a hedgehog agonist, and Wnt ligands – only PDGFB and TGFB had a strong pro-fibrotic effect in microHOs. For several of the cytokines and growth factors tested, the absence of a pro-fibrotic effect in the organoid could be due to the absence of an immune system and/or of other cell types that are required for their pro-fibrotic effect. However, a key finding emerging from this study is that the anti-fibrotic efficacy of PDGFR and TGFBR1 tyrosine kinase inhibitors was dependent upon the factor driving the fibrosis, and this could explain why it has been so difficult to develop liver fibrosis therapies. When fibrosis is driven by PDGFRβ-STAT3 pathway activation – as occurs in ARPKD liver fibrosis (11) or in murine models of lung and bone marrow fibrosis (71) – PDGFR inhibitors will exhibit anti-fibrotic efficacy; but they will be less effective when the fibrosis is driven by other mechanisms. There are organ-specific and species-specific differences in the mechanisms mediating tissue fibrosis (9) and different types

13

of liver injury produces different patterns of liver fibrosis in humans (72). Consistent with these differences, microHO data indicates that at least one (and possibly both) of the FDA approved drugs for treatment of lung fibrosis may not be effective for liver fibrosis. It is also noteworthy that a combination treatment of PDGFR (imatinib) and TGFBR1 (galunisertib (73)) inhibitors was more effective than blockade of either pathway alone in a murine radiation-induced lung fibrosis model (74). Hence, to optimally treat liver fibrosis, therapies may have to be adjusted based upon the pathogenic driving factors, which may vary in different patients or in response to different inciting causes. There is already evidence that Diabetes patients can be subdivided into distinct sub-groups based upon clinical features and biomarker results (75), and efforts are underway to optimize treatment selection for the different types of diabetes patients (76). Just as in other diseases, application of the principles of '*precision medicine'* (i.e., using genetic or genomic information to optimize treatment selection (77)) could enable therapies for liver fibrosis to be successfully developed.

Another key finding was that GSK3β and p38 MAPK inhibitors potently blocked the fibrosis induced by TGFB or PDGFB. The GSK3β inhibitor effect was unexpected since modulating Wnt/β-catenin signaling has had variable effects on liver fibrosis in mouse models (78, 79); and in a murine bile duct ligation model, GSK3β inhibitor administration increased the extent of liver fibrosis (80). As discussed in supplemental note 2, there are multiple nodes where the TGFB, Wnt/β-catenin and the p38 MAPK pathways interact. These interactions could explain how a GSK3β inhibitor could block TGFB-induced fibrosis; but the mechanism for the GSK3β inhibitor effect on PDGFB-induced fibrosis is less clear. Nevertheless, our results indicate that the p38 MAPK pathway, which is activated by both TGFB and PDGFB receptors, plays a key role in fibrosis. Although there was no prior data demonstrating that it had an effect on liver fibrosis, the ability of SB202190 to inhibit fibrosis in microHOs is consistent with prior studies showing that

this agent inhibited the development of renal interstitial (81) and corneal (82) fibrosis in animal models, and it blocked the conversion of human corneal fibroblasts into myofibroblasts *in vitro* (83). However, additional studies will have to be performed to characterize the mechanism(s) by which the Wnt/β-catenin and p38 MAPK pathways, along with the SMAD and STAT3 pathways that are also activated by TGFB and PDGFB receptors, jointly contribute to liver fibrosis. Moreover, microHOs can also be used in conjunction with other recently developed genomic methods to provide a deeper understanding of the mechanisms mediating liver fibrosis (84). In summary, live cell imaging of human microHOs has identified GSK3β and p38 MAPK inhibitors as potential new therapies for liver fibrosis, and it is likely that other new therapies and their mechanism(s) of action could subsequently be identified using this system.

Methods

Chemicals. The growth factors, drugs, antibodies, and other staining reagents are shown in Tables S1-S2.

iPSCs and HO generation. The human iPSC line (C3) used in this study was prepared as previously described (10). The biopsy sample used to generate this iPSC line was obtained according to a protocol (number 10368) approved by the Institutional Review Board at Stanford. The CRISPR-assisted insertion tagging system (CRISPaint) (13) plasmid (pCRISPR-HOT-Clover-BlastR) was obtained from Addgene (Plasmid #138569; http://n2t.net/addgene:138569). A clover expression cassette (**P2A-Clover**) was inserted at the COOH terminus of the endogenous *COL1A1* gene of the iPSC line without a STOP code using a sgRNA (TTGGGATGGAGGGAGTTTAC). After Blasticidin selection, colonies obtained from single cells were picked and genotyped for the correct in-frame insertion using forward (actcccacgtggtaatgccc); and reverse (cttcagggtcagcttgccg) primers. iPSCs were differentiated

15

into hepatic organoids (HOs) via culture in a series of media containing different growth factors using methods (10) that are described below.

Second Harmonic Generation (SHG) microscopy. SHG (collagen fibers) images from day 21 control, PDGF-treated and TGFβ1-treated HOs were collected on a multimodal nonlinear optical microscope setup, consisting of a modified inverted confocal microscope (Nikon, Ti2-E with C2 scanner and 60X water immersion objective, NA=1.27) and a picosecond-pulsed laser source (APE picoEmerald S, 2 ps pulse width, 80 MHz repetition rate, and 10 cm^{-1} bandwidth). As previously described(10), SHG data collection was made in the epi-direction with two narrow bandpass filters (Semrock FF01-400/12, Thorlabs MF390-18) and one shortpass filter (Thorlabs FESH0500). For the quantitative analyses, the area of the collagen fibers (identified by Otsu thresholding) was calculated for each SHG image and divided by the total sample area, forming the collagen area fraction (in %). To determine the diameter of the collagen fibers, the local thickness of the fibers was evaluated by applying the ImageJ Local Thickness routine (see the Analyze menu in Fiji) (85) to the SHG data. The volume fraction of thick collagen fibers (diameter ≥ 3 μm) was estimated by dividing the number of pixels represented by local thickness values ≥ 3 μm by the total number of pixels of the stack. To test whether the volume fractions obtained for control and TGFβ1- or PDGF-treated organoids were significantly different, the Welch's t-test was applied (* $p<0.05$ and ** $p<0.01$).

microHO generation. To produce microHOs, 50~60% confluent iPSC cultures were switched to an endoderm differentiation medium that consisted of DMEM/F12 + ITS (GIBCO) supplemented with 0.1 mM nonessential amino acids, 1 mM pyruvate and 2 mM L-alanyl-L-glutamine dipeptide (GlutaMAX). On days 1 to 2, 100 ng/ml Activin-A (Peprotech, Rocky Hill, NJ), 10 ng/ml BMP4 (Peprotech), 100 ng/ml bFGF (Peprotech), 3 mM CHIR99021

(Selleckchem, Houston, TX) and 10 uM LY294002 (Selleckchem) were added this medium. On day 3, 100 ng/ml Activin-A and 100 ng/ml bFGF were added the definitive endoderm differentiation medium. From days 4 to 9, 20 ng/ml FGF10 (Peprotech) and 20 ng/ml BMP4 were added to the hepatoblast medium, which consisted of which consisted of Advanced RPMI 1640 Medium (Gibco) that was supplemented with GlutaMAX and ITS. After day 9, the hepatoblasts were dissociated to single cells in Accutase (Invitrogen) medium with 10 uM Y-27632 (Santa Cruz Biotechnology, Dallas, Texas). Then, 1000 to 5000 cells/well were re-aggregated in low-cell-adhesion Nunclon™ Sphera™ 96 well Microplates (ThermoFisher) that contained serum-free HO growth and differentiation medium, which consisted of William's E medium supplemented with 0.1% Polyvinyl alcohol (Sigma-Aldrich), 0.1 mM nonessential amino acids, 1 mM pyruvate, 2 mM L-alanyl-L-glutamine dipeptide (GlutaMAX), 10 mM Y-27632, 100 ng/ml EGF, 10 ng/ml HGF, 10 μM Dexamethasone and 10 μM Hydrocortisone (Sigma, St. Louis MO). On day 13, 50 ng/ml of TGFβ1 (Peprotech, 100-21; or Sinobiological, 10804-HNAC) or 50 ng/ml of PDGFB (Miltenyibiotec, 130-108-163; or Peprotech, 100-14B) was added to each microwell.

microHO analysis. For COL1A1$^+$ and Hoechst 33342 (Invitrogen, H3570) fluorescence measurements, 3D stacked images were captured from day 14 to day 31 cultures using a Molecular Devices ImageXpress Micro Confocal system. For confocal imaging20 to 40 planes crossing the whole organoid at 20 um intervals were captured using a 10X 0.45 Plan Apo 4mm WD objective with a 60-um pinhole. For each 10X confocal z-stack field (enough to cover one whole organoid), maximum intensity projections (MIPs) were generated from all of the acquired z-planes (the number planes ranged from 20 to 40 depending on the batch size). MIPs from each channel belonging to the same well were used for organoid segmentation and feature extraction by applying the machine learning based 'Trainable Weka Segmentation' [86] plugin

from FIJI (87). Each individual organoid edge was automatically segmented based on the nuclei signal (Hoechst 33342). Cell numbers were determined using the 'Find Maxima' function in defined area of an organoid after segmentation. COL1A1-P2A-Clover$^+$ cells were segmented based on fluorescence. For training purposes, each analyzed element in every image (total 12 images) were used to train the classifiers by manual labelling all positive spots. Then, for experimental image analysis, the saved classifier was used to generate the probability map for each image. Segmented areas were then isolated, thresholded and binarized, and the Integrated Density was calculated from segmented area. An unpaired Student's t-test was used to test whether the measurements were significantly different between each comparison group. The macro script used for this analysis is available upon request.

Immunoblotting. iPSCs and day 9 hepatoblast cultures, and day 21 control, PDGF- or TGFβ-treated HOs (n=16 per condition) were lysed in RIPA buffer. The lysates were analyzed by PAGE on a 4-15% Tris-glycine gel. After blotting onto a membrane, the membranes were incubated with a 1:2000 dilution of an anti-GFP antibody (Clontech 632381, clone JL8) for detection of Clover protein, and the secondary antibodies were IRDye® 680 and 800 (LI-COR Biosciences).

scRNA-Sequencing. Control, PDGFB- or TGFβ1-induced microHOs (n>30 per group) were harvested from multiple independently prepared sets of cultures, and single cell suspensions were prepared by protease digestion as described (10). The single cell suspensions were visually inspected under a microscope, cells were counted using a Scepter™ 2.0 Handheld Automated Cell Counter (EMD Millipore, Burlington, MA), and then resuspended in PBS with 0.01% BSA. scRNA-seq libraries were prepared by using the spit-pool based scRNA-Seq method (Evercode™ WT Mini v2 from Parse biosciences) according to the manufacturer's

instructions. In brief, ~5,000 cells from each group were split into 3 wells for the first round of

sample barcoding, and the final pooled cells were divided into two equal libraries for

sequencing. The expression matrix was generated using the 'Parse Biosciences analysis

pipeline.' A total of 38,716 features that were generated from 13,160 cells were generated from

four experimental batches, and 57, 7778 cells were recovered that passed quality control for

processing of the scRNA-Seq data.

Flow cytometry iPSCs were dissociated into single cells by incubation with 5 μM ETDA

(Invitrogen) in PBS; and hepatoblasts were dissociated using Accutase (Gibco). Single cell

suspensions were prepared from microHOs by protease digestion as described (10). Flow

cytometry was performed using at a BD Accuri C6 flow cytometer using the conjugated

antibodies listed in Table S2, and the data was analyzed using FCS Express

(denovosoftware.com) software. A density plot of forward scatter height (FSC-H) vs. forward

scatter area (FSC-A) was used to exclude doublets.

scRNA-Seq data analysis. The scRNA-Seq data was imported into 'Seurat' (88) for the

subsequent analysis steps. (i) Cells with unique gene counts <200 or where the percentage of

mitochondrial mRNAs was >10% were removed. (ii) A total of 2000 variable genes were

identified using the default settings. Four batches of data were integrated by standard

processing methods using the Seurat integration function. Unwanted sources of variation were

removed by regression analysis, which was performed to mitigate the effect of signals caused

by mRNAs with unique molecular identifiers and mitochondrial expression. (iii) Ten principal

components were used to construct the shared nearest neighbor (SNN) graph, and the

parameter regulating the resolution of the 'Find Clusters' program, was set to 0.5. This resulted

in the identification of 11 unique clusters for all 57,778 cells. To identify the cell type of each

cluster, differentially expressed genes for the pre-defined cell types were computed using the

'FindAllMarkers' function within the Seurat Package with the following parameters: only.pos =
TRUE, min.pct = 0.25, logfc.threshold = 0.25. Seurat then identifies the differentially expressed
genes using the non-parametric Wilcoxon rank sum test. The top 100 DEGs were used for the
GO biological process analysis, which was performed using the 'clusterProfiler' for GO over-
representation analysis (89).

Module score calculation. Module scores were calculated to assess the relationship between
the transcriptomes of microHO clusters and the different types of cells in human liver tissue.
scRNA-Seq data obtained from normal and cirrhotic human liver tissue (GSE136103) (90) was
used to identify the different types of liver cells. Differentially expressed genes were calculated
for each of the clusters in microHO (MyoF_T1, MyoF_P, Mes2) and human liver tissue
(Myofibroblast, HSC, VSMC and Meso), using the 'FindMarkers' function of the R package in
Seurat (91). Then, each of the gene signatures used for determining the module score were
selected based on the intersection between the marker genes in microHO and those in the cell
types in human liver. There were 53, 84, and 31 shared genes that were used to calculate the
module scores for MyoF_T1 vs MyoF in liver, MyoF_P and liver MyoF, and Mes2 and liver HSC,
respectively. For comparisons of the scores obtained with vascular smooth muscle cells
(VSMC), HSC, Myofibroblasts and Mesothelial cells, a one-way ANOVA was used to compare
the means of the measurements for the four groups. The Tukey multiple comparison of the
means test was then used to determine whether there was a significant difference between the
means of all possible comparisons.

2-way analysis of variance (ANOVA) calculations. The 2-way ANOVA was used to compare
the means of the COL1A1:Clover signal (calculated as area * mean intensity (IntDen)) between
the different drug treatment groups and time points, while also assessing interaction effects
between the treatment groups and time. The two-way ANOVA was performed using the 'aov'

function of the 'R\stats' package, and both groups and time points were analyzed as categorical independent variables. The null hypothesis was that there is no difference in the means of the different treatment groups or timepoints, and that the treatment groups and time points do not interact in any way. Since the two-way ANOVA of the data shown in Figures 2F-G, 6B, 6C, 7A and 7B use separate datasets, a correction for multiple testing is not needed.

RNA velocity, Cytotrace2, cell-cell communication and TF activity analysis. RNA velocity analysis infers cell state by measuring the ratio of un-spliced to spliced mRNA transcripts, which provides information about the transcriptional activity of a gene and its direction. The transcript assignment file (tscp_assignment.csv.gz from the Parse pipeline output directory) contains the splicing information for each transcript identified in a Parse assay. The splicing information is used to generate the splice matrices that are required to run scVelo (41). The Anndata file, which is required for scVelo, was generated using the Seurat object that contains the metadata, and splicing matrix. RNA velocity was estimated with the 'stochastic model' (using second-order moments). Cellular potency categories and the absolute developmental potential was assessed with 'CytoTRACE 2' (42) using the scRNA-seq data. The predicted potency scores provide a continuous measure of developmental potential; and they range from 0 (differentiated) to 1 (totipotent). The raw count from Seurat object is used to directly to compute CytoTRACE score. The R toolkit 'CellChat' v2 was used for inference, visualization and analysis of cell-cell communication based upon the scRNA-seq data (92). The All CellChatDB, except for the "Non-protein signaling" component, was used for analysis of cell-cell communication. The R implementation of 'decoupleR' (45) was used to extract biological activities from the CollecTRI database. CollecTRI is a comprehensive resource containing a curated collection of TFs and their transcriptional targets compiled from 12 different sources *(93)*. The interactions are weighted based upon their mode of regulation (activation or inhibition).

Analysis of drug effect in C1 and C2 microHOs. The C1 and C2 iPSC lines were generated and characterized as previously described (10) and used to prepare microHOs as described above. Trichrome staining of day 21 microHOs was performed according to the manufacturer's instructions using MASSON'S 2000 TRICHROME stain (Americanmastertech, Lodi, CA). Image segmentation and quantitative measurement of collagen rich areas was performed using our previously described methods (11). In brief, Fiji (2.1.0) implementation of ImageJ was used to quantify the areas of positive staining. The 'Trainable Weka Segmentation' plug-in was used to train the classifiers and calculate the test experimental image. Statistical analysis was performed using a one-way ANOVA to assess the overall differences between group means, and Tukey's post-test was then used for pairwise comparisons to identify groups with significant differences in their means.

Statistical overview. For analysis of the volume fractions obtained for control and TGFβ1- or PDGF-treated organoids in SHG images were significantly different, the Welch's t-test was applied with cutoffs of * $p<0.05$ and ** $p<0.01$. For comparing the effect of drugs on fibrosis in microHOs, a 2-way ANOVA was used to compare the means of the COL1A1:Clover signal (calculated as area * mean intensity (IntDen)) between the different drug treatment groups and time points, while also assessing interaction effects between the treatment groups and time. Statistical analysis of drug effects on fibrosis in C1 and C2 HOs was performed using a one-way ANOVA to assess the overall differences between group means, and Tukey's post-test was then used for pairwise comparisons to identify groups with significant differences in their means.

Study approval. The iPSC were prepared according to a protocol (#10368) that was approved by the Institutional Review Board at the Stanford University School of Medicine (Stanford, CA).

References

1. Iyer SN, Gurujeyalakshmi G, and Giri SN. Effects of pirfenidone on transforming growth factor-beta gene expression at the transcriptional level in bleomycin hamster model of lung fibrosis. *J Pharmacol Exp Ther.* 1999;291(1):367-73.
2. Pinzani M, and Luong TV. Pathogenesis of biliary fibrosis. *Biochim Biophys Acta Mol Basis Dis.* 2018;1864(4 Pt B):1279-83.
3. Pinzani M. Pathophysiology of Liver Fibrosis. *Dig Dis.* 2015;33(4):492-7.
4. Zhang CY, Yuan WG, He P, Lei JH, and Wang CX. Liver fibrosis and hepatic stellate cells: Etiology, pathological hallmarks and therapeutic targets. *World J Gastroenterol.* 2016;22(48):10512-22.
5. Tsuchida T, and Friedman SL. Mechanisms of hepatic stellate cell activation. *Nature reviews Gastroenterology & hepatology.* 2017;14(7):397-411.
6. Yin C, Evason KJ, Asahina K, and Stainier DY. Hepatic stellate cells in liver development, regeneration, and cancer. *J Clin Invest.* 2013;123(5):1902-10.
7. Zhang DY, Goossens N, Guo J, Tsai MC, Chou HI, Altunkaynak C, et al. A hepatic stellate cell gene expression signature associated with outcomes in hepatitis C cirrhosis and hepatocellular carcinoma after curative resection. *Gut.* 2016;65(10):1754-64.
8. Mederacke I, Hsu CC, Troeger JS, Huebener P, Mu X, Dapito DH, et al. Fate tracing reveals hepatic stellate cells as dominant contributors to liver fibrosis independent of its aetiology. *Nature communications.* 2013;4:2823.
9. Mehal WZ, Iredale J, and Friedman SL. Scraping fibrosis: expressway to the core of fibrosis. *Nat Med.* 2011;17(5):552-3.

10. Guan Y, Xu D, Garfin PM, Ehmer U, Hurwitz M, Enns G, et al. Human Hepatic Organoids for the Analysis of Human Genetic Diseases. *JCI Insight.* 2017;2(17):pii: 94954.
11. Guan Y, Enejder A, Wang M, Fang Z, Cui L, Chen SY, et al. A human multi-lineage hepatic organoid model for liver fibrosis. *Nature communications.* 2021;12(1):6138.
12. Hernandez-Gea V, and Friedman SL. Pathogenesis of liver fibrosis. *Annual review of pathology.* 2011;6:425-56.
13. Schmid-Burgk JL, Honing K, Ebert TS, and Hornung V. CRISPaint allows modular base-specific gene tagging using a ligase-4-dependent mechanism. *Nature communications.* 2016;7:12338.
14. Campagnola PJ, and Loew LM. Second-harmonic imaging microscopy for visualizing biomolecular arrays in cells, tissues and organisms. *Nat Biotechnol.* 2003;21(11):1356-60.
15. Deniset-Besseau A, Duboisset J, Benichou E, Hache F, Brevet PF, and Schanne-Klein MC. Measurement of the second-order hyperpolarizability of the collagen triple helix and determination of its physical origin. *J Phys Chem B.* 2009;113(40):13437-45.
16. Sun W, Chang S, Tai DC, Tan N, Xiao G, Tang H, et al. Nonlinear optical microscopy: use of second harmonic generation and two-photon microscopy for automated quantitative liver fibrosis studies. *J Biomed Opt.* 2008;13(6):064010.
17. Gailhouste L, Le Grand Y, Odin C, Guyader D, Turlin B, Ezan F, et al. Fibrillar collagen scoring by second harmonic microscopy: a new tool in the assessment of liver fibrosis. *J Hepatol.* 2010;52(3):398-406.
18. Yamauchi M, and Sricholpech M. Lysine post-translational modifications of collagen. *Essays Biochem.* 2012;52:113-33.
19. Laping NJ, Grygielko E, Mathur A, Butter S, Bomberger J, Tweed C, et al. Inhibition of transforming growth factor (TGF)-beta1-induced extracellular matrix with a novel inhibitor of the TGF-beta type I receptor kinase activity: SB-431542. *Mol Pharmacol.* 2002;62(1):58-64.
20. Inman GJ, Nicolas FJ, Callahan JF, Harling JD, Gaster LM, Reith AD, et al. SB-431542 is a potent and specific inhibitor of transforming growth factor-beta superfamily type I activin receptor-like kinase (ALK) receptors ALK4, ALK5, and ALK7. *Mol Pharmacol.* 2002;62(1):65-74.
21. Tojo M, Hamashima Y, Hanyu A, Kajimoto T, Saitoh M, Miyazono K, et al. The ALK-5 inhibitor A-83-01 inhibits Smad signaling and epithelial-to-mesenchymal transition by transforming growth factor-beta. *Cancer Sci.* 2005;96(11):791-800.
22. Breedveld P, Pluim D, Cipriani G, Wielinga P, van Tellingen O, Schinkel AH, et al. The Effect of Bcrp1 (Abcg2) on the In vivo Pharmacokinetics and Brain Penetration of Imatinib Mesylate (Gleevec): Implications for the Use of Breast Cancer Resistance Protein and P-Glycoprotein Inhibitors to Enable the Brain Penetration of Imatinib in Patients. *Cancer Research.* 2005;65(7):2577-82.
23. Weng SY, Wang X, Vijayan S, Tang Y, Kim YO, Padberg K, et al. IL-4 Receptor Alpha Signaling through Macrophages Differentially Regulates Liver Fibrosis Progression and Reversal. *EBioMedicine.* 2018;29:92-103.
24. Paquissi FC. Immunity and Fibrogenesis: The Role of Th17/IL-17 Axis in HBV and HCV-induced Chronic Hepatitis and Progression to Cirrhosis. *Front Immunol.* 2017;8:1195.
25. Marvie P, Lisbonne M, L'Helgoualc'h A, Rauch M, Turlin B, Preisser L, et al. Interleukin-33 overexpression is associated with liver fibrosis in mice and humans. *J Cell Mol Med.* 2010;14(6B):1726-39.
26. Tan Z, Liu Q, Jiang R, Lv L, Shoto SS, Maillet I, et al. Interleukin-33 drives hepatic fibrosis through activation of hepatic stellate cells. *Cell Mol Immunol.* 2018;15(4):388-98.

27.	Lu S, Wang Y, and Liu J. Tumor necrosis factor-alpha signaling in nonalcoholic steatohepatitis and targeted therapies. *J Genet Genomics.* 2022;49(4):269-78.
28.	Adamek A, and Kasprzak A. Insulin-Like Growth Factor (IGF) System in Liver Diseases. *International journal of molecular sciences.* 2018;19(5).
29.	Mariotti V, Fiorotto R, Cadamuro M, Fabris L, and Strazzabosco M. New insights on the role of vascular endothelial growth factor in biliary pathophysiology. *JHEP Rep.* 2021;3(3):100251.
30.	Xu L, Chen Y, Nagashimada M, Ni Y, Zhuge F, Chen G, et al. CC chemokine ligand 3 deficiency ameliorates diet-induced steatohepatitis by regulating liver macrophage recruitment and M1/M2 status in mice. *Metabolism: clinical and experimental.* 2021;125:154914.
31.	Choi SS, Omenetti A, Syn WK, and Diehl AM. The role of Hedgehog signaling in fibrogenic liver repair. *Int J Biochem Cell Biol.* 2011;43(2):238-44.
32.	Syn WK, Jung Y, Omenetti A, Abdelmalek M, Guy CD, Yang L, et al. Hedgehog-mediated epithelial-to-mesenchymal transition and fibrogenic repair in nonalcoholic fatty liver disease. *Gastroenterology.* 2009;137(4):1478-88 e8.
33.	Chen JK, Taipale J, Cooper MK, and Beachy PA. Inhibition of Hedgehog signaling by direct binding of cyclopamine to Smoothened. *Genes Dev.* 2002;16(21):2743-8.
34.	Taipale J, Chen JK, Cooper MK, Wang B, Mann RK, Milenkovic L, et al. Effects of oncogenic mutations in Smoothened and Patched can be reversed by cyclopamine. *Nature.* 2000;406(6799):1005-9.
35.	Chen JK, Taipale J, Young KE, Maiti T, and Beachy PA. Small molecule modulation of Smoothened activity. *Proc Natl Acad Sci U S A.* 2002;99(22):14071-6.
36.	Levy MT, McCaughan GW, Marinos G, and Gorrell MD. Intrahepatic expression of the hepatic stellate cell marker fibroblast activation protein correlates with the degree of fibrosis in hepatitis C virus infection. *Liver.* 2002;22(2):93-101.
37.	Gorrell MD, Wang XM, Levy MT, Kable E, Marinos G, Cox G, et al. Intrahepatic expression of collagen and fibroblast activation protein (FAP) in hepatitis C virus infection. *Adv Exp Med Biol.* 2003;524:235-43.
38.	Lay AJ, Zhang HE, McCaughan GW, and Gorrell MD. Fibroblast activation protein in liver fibrosis. *Front Biosci (Landmark Ed).* 2019;24(1):1-17.
39.	Yang AT, Kim YO, Yan XZ, Abe H, Aslam M, Park KS, et al. Fibroblast Activation Protein Activates Macrophages and Promotes Parenchymal Liver Inflammation and Fibrosis. *Cell Mol Gastroenterol Hepatol.* 2022;15(4):841-67.
40.	Mangiola S, Roth-Schulze AJ, Trussart M, Zozaya-Valdes E, Ma M, Gao Z, et al. sccomp: Robust differential composition and variability analysis for single-cell data. *Proc Natl Acad Sci U S A.* 2023;120(33):e2203828120.
41.	Bergen V, Lange M, Peidli S, Wolf FA, and Theis FJ. Generalizing RNA velocity to transient cell states through dynamical modeling. *Nat Biotechnol.* 2020;38(12):1408-14.
42.	Kang M, Armenteros JJA, Gulati GS, Gleyzer R, Avagyan S, Brown EL, et al. Mapping single-cell developmental potential in health and disease with interpretable deep learning. *bioRxiv.* 2024.
43.	Subramanian A, Tamayo P, Mootha VK, Mukherjee S, Ebert BL, Gillette MA, et al. Gene set enrichment analysis: a knowledge-based approach for interpreting genome-wide expression profiles. *Proc Natl Acad Sci U S A.* 2005;102(43):15545-50.
44.	Jin S, Guerrero-Juarez CF, Zhang L, Chang I, Ramos R, Kuan CH, et al. Inference and analysis of cell-cell communication using CellChat. *Nature communications.* 2021;12(1):1088.
45.	Badia IMP, Velez Santiago J, Braunger J, Geiss C, Dimitrov D, Muller-Dott S, et al. decoupleR: ensemble of computational methods to infer biological activities from omics data. *Bioinform Adv.* 2022;2(1):vbac016.

46.   Frangogiannis N. Transforming growth factor-beta in tissue fibrosis. *J Exp Med.* 2020;217(3):e20190103.

47.   Zhang YE. Non-Smad Signaling Pathways of the TGF-beta Family. *Cold Spring Harbor perspectives in biology.* 2017;9(2).

48.   Budi EH, Duan D, and Derynck R. Transforming Growth Factor-beta Receptors and Smads: Regulatory Complexity and Functional Versatility. *Trends Cell Biol.* 2017;27(9):658-72.

49.   Vignais ML, and Gilman M. Distinct mechanisms of activation of Stat1 and Stat3 by platelet-derived growth factor receptor in a cell-free system. *Mol Cell Biol.* 1999;19(5):3727-35.

50.   Ying HZ, Chen Q, Zhang WY, Zhang HH, Ma Y, Zhang SZ, et al. PDGF signaling pathway in hepatic fibrosis pathogenesis and therapeutics (Review). *Mol Med Rep.* 2017;16(6):7879-89.

51.   Budi EH, Schaub JR, Decaris M, Turner S, and Derynck R. TGF-beta as a driver of fibrosis: physiological roles and therapeutic opportunities. *J Pathol.* 2021;254(4):358-73.

52.   Razmara M, Heldin CH, and Lennartsson J. Platelet-derived growth factor-induced Akt phosphorylation requires mTOR/Rictor and phospholipase C-gamma1, whereas S6 phosphorylation depends on mTOR/Raptor and phospholipase D. *Cell Commun Signal.* 2013;11(1):3.

53.   Pan S, Hu Y, Hu M, Jian H, Chen M, Gan L, et al. Platelet-derived PDGF promotes the invasion and metastasis of cholangiocarcinoma by upregulating MMP2/MMP9 expression and inducing EMT via the p38/MAPK signalling pathway. *Am J Transl Res.* 2020;12(7):3577-95.

54.   Frantz B, Klatt T, Pang M, Parsons J, Rolando A, Williams H, et al. The activation state of p38 mitogen-activated protein kinase determines the efficiency of ATP competition for pyridinylimidazole inhibitor binding. *Biochemistry.* 1998;37(39):13846-53.

55.   Finnerty JP, Ponnuswamy A, Dutta P, Abdelaziz A, and Kamil H. Efficacy of antifibrotic drugs, nintedanib and pirfenidone, in treatment of progressive pulmonary fibrosis in both idiopathic pulmonary fibrosis (IPF) and non-IPF: a systematic review and meta-analysis. *BMC Pulm Med.* 2021;21(1):411.

56.   Wollin L, Wex E, Pautsch A, Schnapp G, Hostettler KE, Stowasser S, et al. Mode of action of nintedanib in the treatment of idiopathic pulmonary fibrosis. *Eur Respir J.* 2015;45(5):1434-45.

57.   Richeldi L, du Bois RM, Raghu G, Azuma A, Brown KK, Costabel U, et al. Efficacy and safety of nintedanib in idiopathic pulmonary fibrosis. *N Engl J Med.* 2014;370(22):2071-82.

58.   Flaherty KR, Wells AU, Cottin V, Devaraj A, Walsh SLF, Inoue Y, et al. Nintedanib in Progressive Fibrosing Interstitial Lung Diseases. *N Engl J Med.* 2019;381(18):1718-27.

59.   Richeldi L, Costabel U, Selman M, Kim DS, Hansell DM, Nicholson AG, et al. Efficacy of a tyrosine kinase inhibitor in idiopathic pulmonary fibrosis. *N Engl J Med.* 2011;365(12):1079-87.

60.   Lancaster LH, de Andrade JA, Zibrak JD, Padilla ML, Albera C, Nathan SD, et al. Pirfenidone safety and adverse event management in idiopathic pulmonary fibrosis. *Eur Respir Rev.* 2017;26(146).

61.   Costabel U, Albera C, Lancaster LH, Lin CY, Hormel P, Hulter HN, et al. An Open-Label Study of the Long-Term Safety of Pirfenidone in Patients with Idiopathic Pulmonary Fibrosis (RECAP). *Respiration.* 2017;94(5):408-15.

62.   Wollin L, Maillet I, Quesniaux V, Holweg A, and Ryffel B. Antifibrotic and anti-inflammatory activity of the tyrosine kinase inhibitor nintedanib in experimental models of lung fibrosis. *J Pharmacol Exp Ther.* 2014;349(2):209-20.

63. Lin X, Yu M, Wu K, Yuan H, and Zhong H. Effects of pirfenidone on proliferation, migration, and collagen contraction of human Tenon's fibroblasts in vitro. *Invest Ophthalmol Vis Sci.* 2009;50(8):3763-70.
64. Hilberg F, Roth GJ, Krssak M, Kautschitsch S, Sommergruber W, Tontsch-Grunt U, et al. BIBF 1120: triple angiokinase inhibitor with sustained receptor blockade and good antitumor efficacy. *Cancer Res.* 2008;68(12):4774-82.
65. Annunziato S, Sun T, and Tchorz JS. The RSPO-LGR4/5-ZNRF3/RNF43 module in liver homeostasis, regeneration, and disease. *Hepatology.* 2022;76(3):888-99.
66. Perugorria MJ, Olaizola P, Labiano I, Esparza-Baquer A, Marzioni M, Marin JJG, et al. Wnt-beta-catenin signalling in liver development, health and disease. *Nature reviews Gastroenterology & hepatology.* 2019;16(2):121-36.
67. Tian L, Wang Y, and Jang YY. Wnt signaling in biliary development, proliferation, and fibrosis. *Exp Biol Med (Maywood).* 2022;247(4):360-7.
68. MacDonald BT, Tamai K, and He X. Wnt/beta-catenin signaling: components, mechanisms, and diseases. *Dev Cell.* 2009;17(1):9-26.
69. Nusse R, and Clevers H. Wnt/beta-Catenin Signaling, Disease, and Emerging Therapeutic Modalities. *Cell.* 2017;169(6):985-99.
70. Sato N, Meijer L, Skaltsounis L, Greengard P, and Brivanlou AH. Maintenance of pluripotency in human and mouse embryonic stem cells through activation of Wnt signaling by a pharmacological GSK-3-specific inhibitor. *Nat Med.* 2004;10(1):55-63.
71. Decker M, Martinez-Morentin L, Wang G, Lee Y, Liu Q, Leslie J, et al. Leptin-receptor-expressing bone marrow stromal cells are myofibroblasts in primary myelofibrosis. *Nat Cell Biol.* 2017;19(6):677-88.
72. Friedman SL, and Pinzani M. Hepatic fibrosis 2022: Unmet needs and a blueprint for the future. *Hepatology.* 2022;75(2):473-88.
73. Yingling JM, McMillen WT, Yan L, Huang H, Sawyer JS, Graff J, et al. Preclinical assessment of galunisertib (LY2157299 monohydrate), a first-in-class transforming growth factor-beta receptor type I inhibitor. *Oncotarget.* 2018;9(6):6659-77.
74. Dadrich M, Nicolay NH, Flechsig P, Bickelhaupt S, Hoeltgen L, Roeder F, et al. Combined inhibition of TGFbeta and PDGF signaling attenuates radiation-induced pulmonary fibrosis. *Oncoimmunology.* 2016;5(5):e1123366.
75. Ahlqvist E, Storm P, Karajamaki A, Martinell M, Dorkhan M, Carlsson A, et al. Novel subgroups of adult-onset diabetes and their association with outcomes: a data-driven cluster analysis of six variables. *Lancet Diabetes Endocrinol.* 2018;6(5):361-9.
76. Perreault L, Skyler JS, and Rosenstock J. Novel therapies with precision mechanisms for type 2 diabetes mellitus. *Nat Rev Endocrinol.* 2021;17(6):364-77.
77. Zeggini E, Gloyn AL, Barton AC, and Wain LV. Translational genomics and precision medicine: Moving from the lab to the clinic. *Science.* 2019;365(6460):1409-13.
78. Zhuang S, Hua X, He K, Zhou T, Zhang J, Wu H, et al. Inhibition of GSK-3beta induces AP-1-mediated osteopontin expression to promote cholestatic liver fibrosis. *FASEB J.* 2018;32(8):4494-503.
79. Pradhan-Sundd T, Kosar K, Saggi H, Zhang R, Vats R, Cornuet P, et al. Wnt/beta-Catenin Signaling Plays a Protective Role in the Mdr2 Knockout Murine Model of Cholestatic Liver Disease. *Hepatology.* 2020;71(5):1732-49.
80. Thompson MD, Moghe A, Cornuet P, Marino R, Tian J, Wang P, et al. beta-Catenin regulation of farnesoid X receptor signaling and bile acid metabolism during murine cholestasis. *Hepatology.* 2018;67(3):955-71.
81. Prakash J, Sandovici M, Saluja V, Lacombe M, Schaapveld RQ, de Borst MH, et al. Intracellular delivery of the p38 mitogen-activated protein kinase inhibitor SB202190 [4-(4-fluorophenyl)-2-(4-hydroxyphenyl)-5-(4-pyridyl)1H-imidazole] in renal tubular cells: a novel strategy to treat renal fibrosis. *J Pharmacol Exp Ther.* 2006;319(1):8-19.

82.   Nassar K, Tura A, Luke J, Luke M, Grisanti S, and Grisanti S. A p38 MAPK inhibitor improves outcome after glaucoma filtration surgery. *J Glaucoma.* 2015;24(2):165-78.

83.   Guo X, Sriram S, Tran JA, Hutcheon AEK, and Zieske JD. Inhibition of Human Corneal Myofibroblast Formation. *Invest Ophthalmol Vis Sci.* 2018;59(8):3511-20.

84.   Guan Y, and Peltz G. Hepatic Organoids Move from Adolescence to Maturity. *Liver International.* 2024;DOI: 10.1111/liv.15893.

85.   Hildebrand T, and Ruegsegger P. A new method for the model-independent assessment of thickness in three-dimensional images. *J of Microscopy.* 1996;185:67-75.

86.   Arganda-Carreras I, Kaynig V, Rueden C, Eliceiri KW, Schindelin J, Cardona A, et al. Trainable Weka Segmentation: a machine learning tool for microscopy pixel classification. *Bioinformatics.* 2017;33(15):2424-6.

87.   Schindelin J, Arganda-Carreras I, Frise E, Kaynig V, Longair M, Pietzsch T, et al. Fiji: an open-source platform for biological-image analysis. *Nat Methods.* 2012;9(7):676-82.

88.   Butler A, Hoffman P, Smibert P, Papalexi E, and Satija R. Integrating single-cell transcriptomic data across different conditions, technologies, and species. *Nat Biotechnol.* 2018;36(5):411-20.

89.   Wu T, Hu E, Xu S, Chen M, Guo P, Dai Z, et al. clusterProfiler 4.0: A universal enrichment tool for interpreting omics data. *Innovation (Camb).* 2021;2(3):100141.

90.   Ramachandran P, Dobie R, Wilson-Kanamori JR, Dora EF, Henderson BEP, Luu NT, et al. Resolving the fibrotic niche of human liver cirrhosis at single-cell level. *Nature.* 2019;575(7783):512-8.

91.   Hao Y, Stuart T, Kowalski MH, Choudhary S, Hoffman P, Hartman A, et al. Dictionary learning for integrative, multimodal and scalable single-cell analysis. *Nat Biotechnol.* 2023.

92.   Jin S, Plikus MV, and Nie Q. CellChat for systematic analysis of cell-cell communication from single-cell and spatially resolved transcriptomics. *BioRxiv.* 2023:2023.11.05.565674.

93.   Muller-Dott S, Tsirvouli E, Vazquez M, Ramirez Flores RO, Badia IMP, Fallegger R, et al. Expanding the coverage of regulons from high-confidence prior knowledge for accurate estimation of transcription factor activities. *Nucleic Acids Res.* 2023;51(20):10934-49.
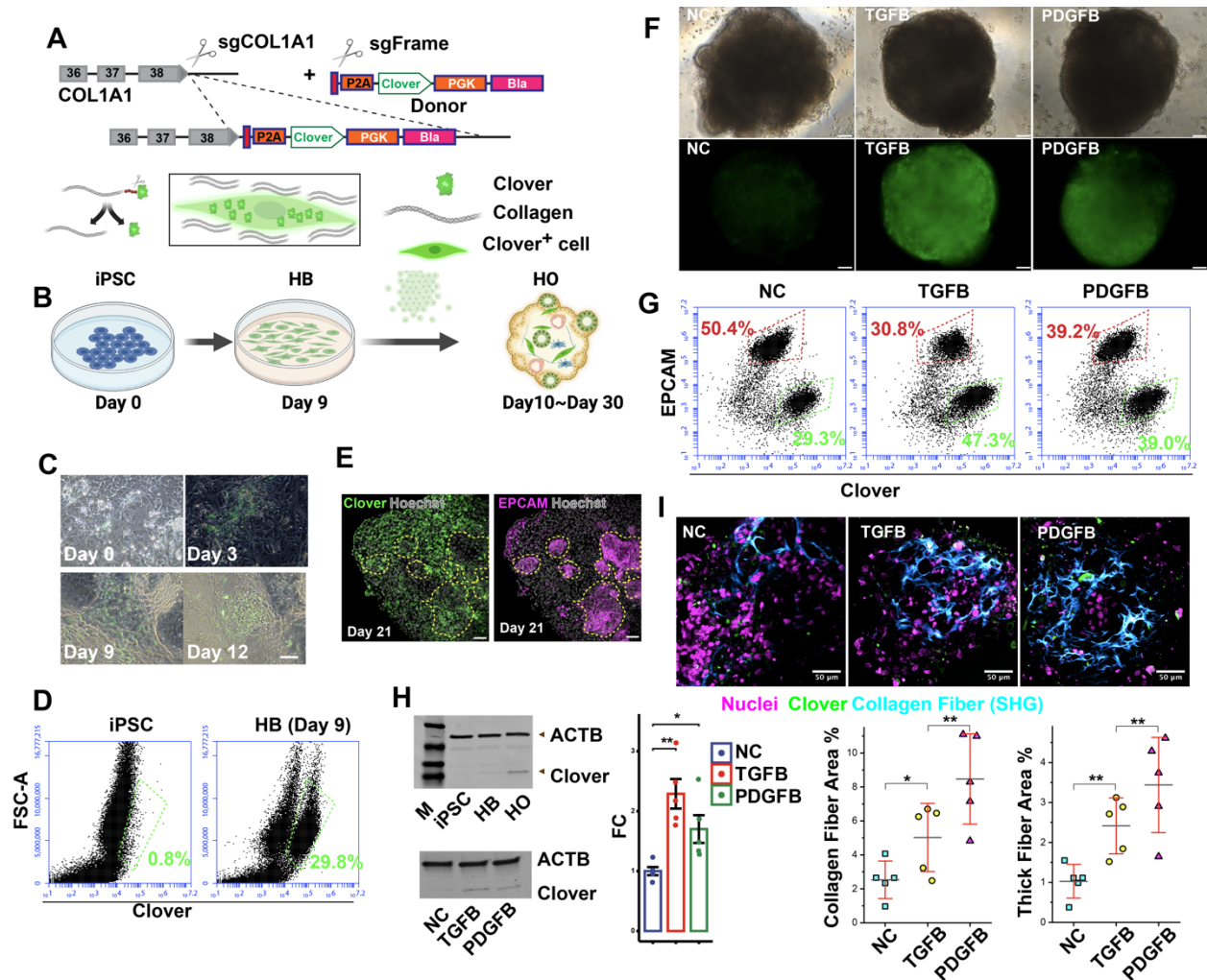
Figure 1. Generation of the COL1A1-P2A-Clover iPSC line used to monitor hepatic fibrosis. **(A)** *Top:* A diagram of the CRISPaint system used to insert P2A-Clover at the 3' end of *COL1A1* in an iPSC line. After blasticidin selection, cells were cloned to generate the COL1A1-P2A-Clover iPSC line. *Bottom*: The self-cleaving P2A peptide enables *COL1A1* expressing cells to be labelled with a fluorescent intracellular protein (Clover). (**B**) The collagen producing cells in a HO produced from COL1A1-P2A-Clover iPSCs are labelled with an intracellular fluorescent Clover protein. (**C**) An overlay of bright field and fluorescent images of differentiating COL1A1-P2A Clover HO cultures reveals that the number of Clover^{+} cells increase between days 3 and 12. Scale bar: 50 μm. (**D**) Flow cytometry scatter plots show that the Clover[+] cell population is absent in iPSC (day 0) but appears in (day 9) hepatoblasts in differentiating *COL1A1*-P2A Clover HO cultures. (**E**) Stacked confocal images show the location of antibody-stained fluorescent Clover[+] (left) or EPCAM[+] (right) cells in day 20 COL1A1-P2A-Clover organoids. The yellow dashed circles (bottom) indicate areas with EPCAM[+] (i.e.,

29

hepatocytes or cholangiocytes) cells; and Clover^{+} cells are not found within those areas but are present in other areas of the HO. Scale bar: 50 μm. (**F**) Bright field (top) and fluorescence (bottom) images of day 21 *COL1A1*-P2A Clover HOs treated on day 13 with no addition (NC), 50 ng/ml TGFB or 50 ng/ml PDGFB. Both growth factors induced a marked increase in COL1A1^{+} cells. Scale bars, 50 μm. (**G**) Flow cytometry scatter plots show that Clover^{+} cells are increased in mature day 21 *COL1A1*-P2A Clover HOs after TGFB or PDGFB exposure. Also, the Clover^{+} cells are distinct from the EPCAM[+] (hepatocytes or cholangiocytes) cells in the HOs. (**H**) Immunoblot showing Clover protein expression in differentiating HO cultures (iPSC, day 9 hepatoblasts (HB)); and in day 21 control (NC), PDGFB- or TGFB-treated HOs. The positions of Clover and β-actin (ACTB) proteins are indicated. Right: This bar plot shows the fold change in the normalized level of Clover protein expression (relative to that in control HOs, Each datapoint is the average of 5 experimental repeats. (**I**) SHG analysis of the collagen fibers formed in human HOs. *Top:* Depth color-coded projections of collagen fibers within day 21 control organoids, or day 21 organoids that were treated with 50 ng/ml TGFB or 50 ng/ml PDGFB on day 13. Control organoids (left) have isolated regions with relatively thin collagen fibers (shown in blue). In contrast, the TGFB or PDGFB-treated organoids form a network of thick collagen fibers that extend throughout the entire organoid. Collagen producing cells (green) can also be seen in these images. Scale bars, 50 μ. *Bottom:* A quantitative comparison of collagen fiber area in SHG images was performed for control, TGFB- or PDGFB-treated hepatic organoids (n = 5 per measurement) on day 21. There is a statistically significant increase in total collagen abundance (collagen fiber area=total area with collagen fibers/area of the imaged organoids) in the organoids after exposure to TGFB (*, $p < 0.05$) or PDGFB (**, $p < 0.01$, Welch t-test). There was also a statistically significant increase in the abundance of thick collagen fibers (i.e., those fibers > 3 um diameter) in the TGFB and PDGFB-treated hepatic organoids.
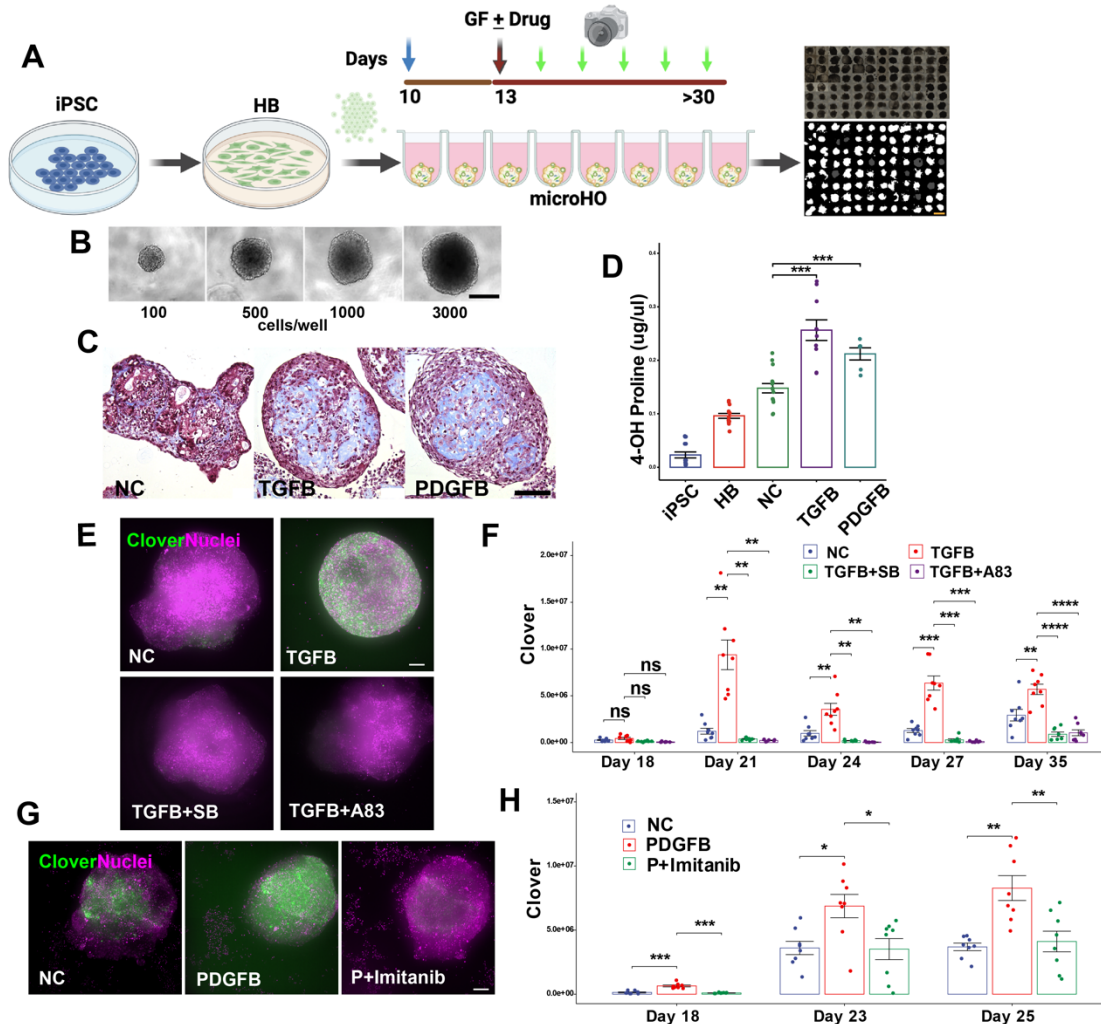
Figure 2. Establishment of a high content imaging platform for anti-fibrotic drug screening. (**A**) A diagram of the HCS platform used for analysis of microHOs. COL1A1-P2A iPSCs are differentiated into hepatoblasts (HB), and 10,000 HBs are placed in each microwell on day 10. Growth factors (GF) and/or drugs are added on day 13, and the cultures are differentiated into hepatic organoids. Culture fluorescence is serially assessed to measure the number of COL1A1-producing cells in the microHO. Bright field (top) and fluorescence (bottom) images of a microwell plate with microHOs is shown on the right. Scale bar, 1 mm. (**B**) A cell number titration experiment was performed by adding the indicated numbers of HBs to microwells and the cells were differentiated through day 12. Bright field images on day 12 reveal that microHOs have a uniform shape and their size is dependent upon the number of input cells. Scale bar, 100 um. (**C**) Trichrome staining reveals a marked increase in collagen (blue areas) in PDGFB or TGFB-treated microHOs relative to control (NC) microHOs. Scale bar, 50 um. (**D**) The 4-Hydroxy-proline (4OH-Proline) concentration was measured in differentiating HO cultures

31

(iPSC, day 9 HB); and in day 21 control (NC), PDGFB- or TGFB-treated HOs. The bar graph shows the mean $\pm$ SE of measurements performed on a total of 15 HOs, which were generated in two separate experiments. There was a statistically significant increase in 4-OH-Proline in the PDGFB- or TGFB-treated day 21 HOs (***, p <0.001 vs NC, t-test). (**E**) Maximum intensity projection (MIP) images of z stack sections obtained from the indicated type of microHOs on day 21. Scale bar 100 um. Clover expression is green, and nuclei stained with Hoechst 33342 are purple. (**F**) TGFB-induced fibrosis in microHOs is blocked by TGFBR1 inhibitors. COL1A1-P2A Clover HOs were formed by adding 10,000 HBs to each microwell. Then, either nothing (NC), or 50 ng/ml TGFB $\pm$ 10 uM TGFBR1 inhibitors (SB431542 (SB) or A83-01 (A83)) was added to each microwell on day 13. The amount of COL1A1$^+$ cells within a microHO were serially measured on days 18 through 21. Each dot represents a measurement made on one microHO, and 8 microHOs per treatment were assessed per condition. A two-way ANOVA indicates that drug treatment and time are two variables that have a significant interaction on the fluorescence measurements (p=1.66 x 10^{-15}) (**Table S9**). (**G**) Representative Maximum intensity projection (MIP) images obtained from the indicated type of microHO on day 21. Scale bar, 100 um.   (**H**) The PDGFB-induced increase in COL1A1$^+$ cells is blocked by a PDGFRβ inhibitor. 50 ng/ml PDGFB (P) or 50 ng/ml PDGFB with 10 μM imatinib was added to each microHO on day 13. The significance indicators are ns, not significant; *, p<0.05; **, p<0.01; ***, p<0.001 or ****, p<0.0001.
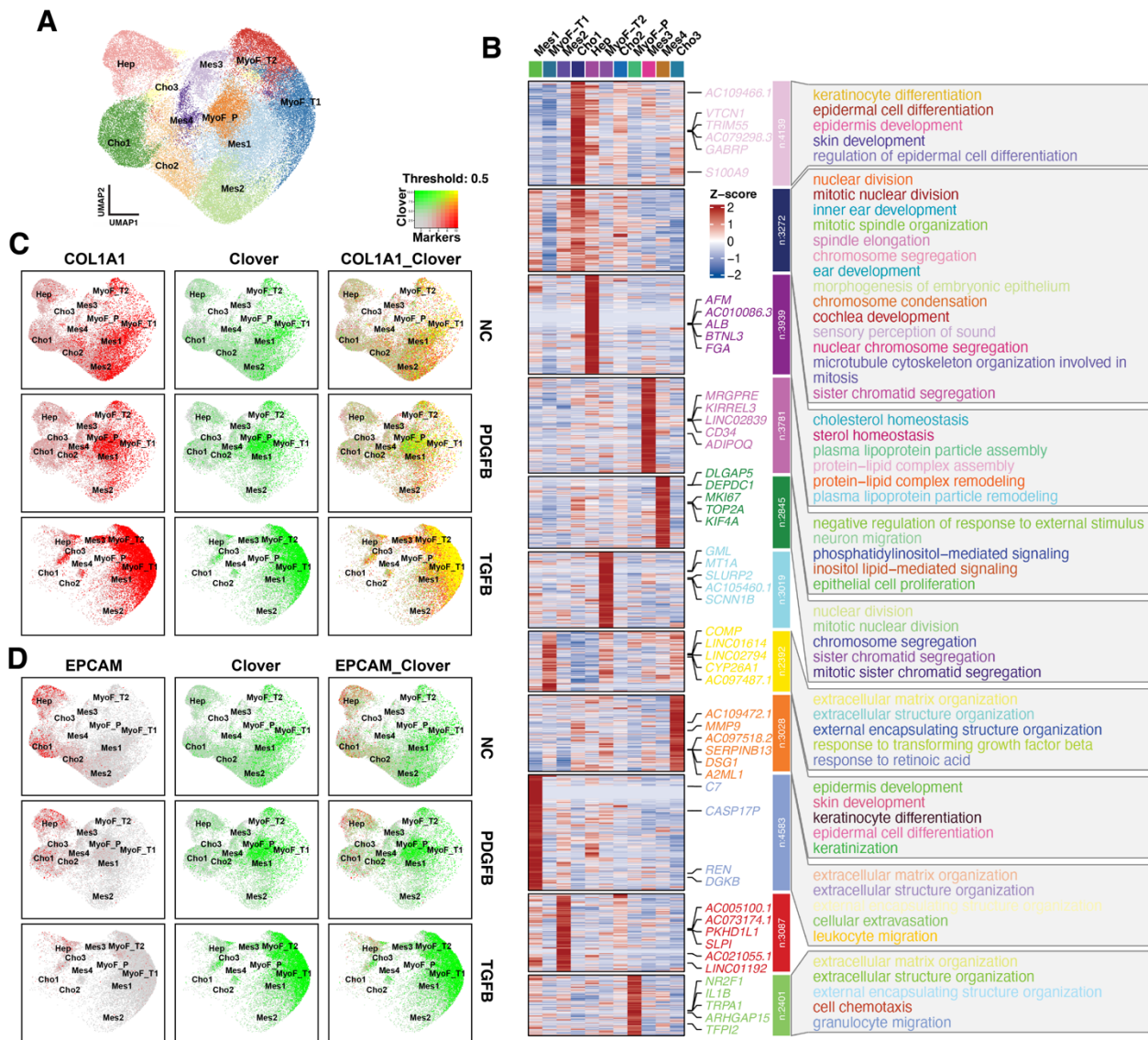
Figure 3 scRNA-seq profiles mHO and *reveal the Clover⁺ population represents mesenchymal.* (**A**) A combined sample UMAP plot shows the 11 cell clusters identified in day 21 control (NC), PDGFB- (P) and TGFB (T)-treated microHO cultures. (**B**) Heatmaps show the differentially expressed genes (DEGs), and the annotated genome ontology pathways identified for each cluster. (**C, D**) These feature plots show the level of expression of *COL1A1* and *Clover* mRNAs (D), or *EPCAM* and *Clover* mRNAs (E) in the UMAP plot shown in (A). As shown in the color threshold diagram, dot colors represent level of mRNA expression. *COL1A1 and Clover* mRNAs have an overlapping expression pattern; they are predominantly expressed in myofibroblasts, and in mesenchymal cells. In contrast, *EPCAM* mRNA is expressed in the hepatocyte and cholangiocyte clusters; and its expression does not overlap with that of *Clover* mRNA.
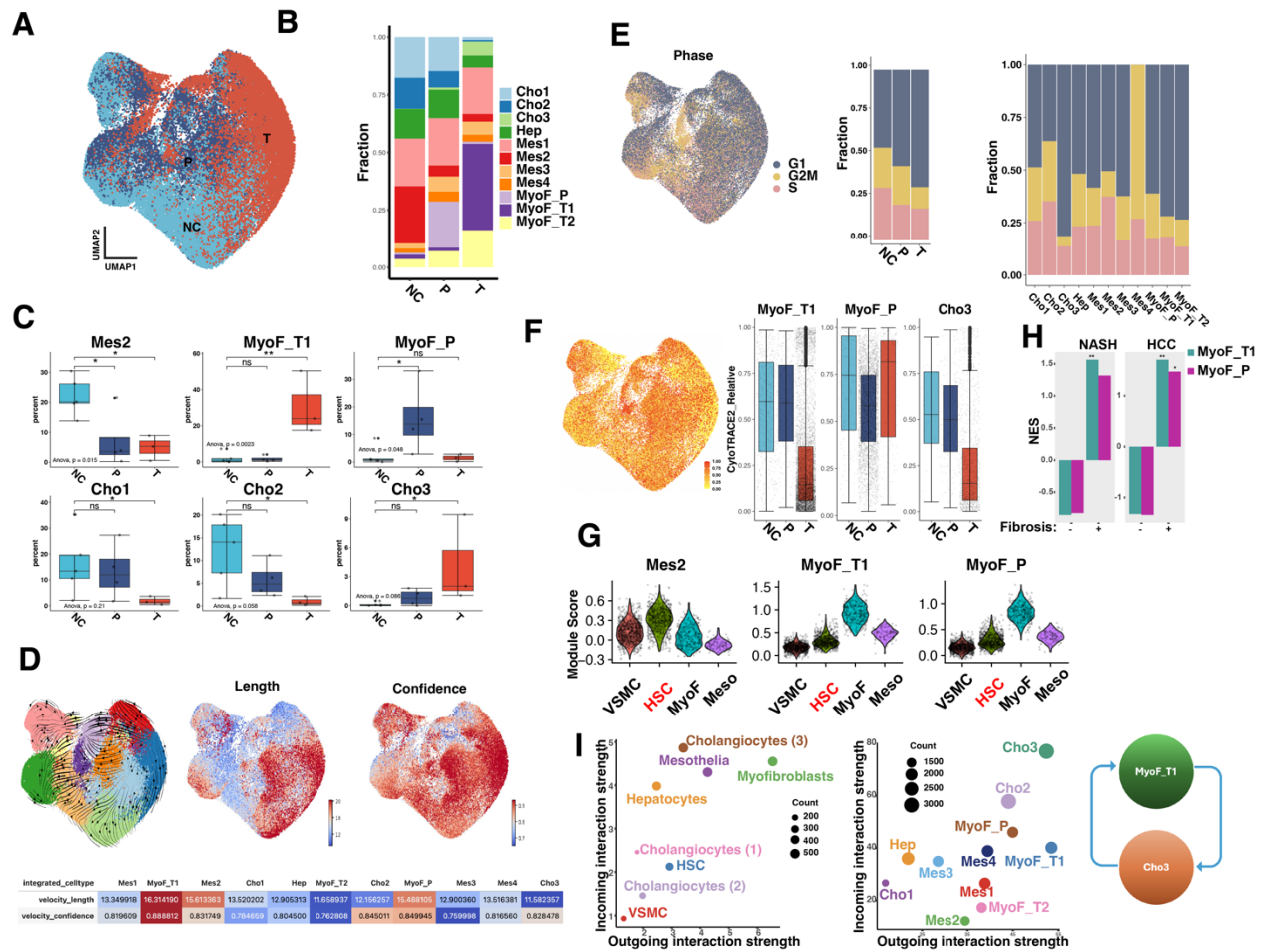
Figure 4. scRNA-seq reveal the PDGFB and TGFB-induced cellular composition *changes in mesenchymal and epithelial cell clusters in fibrotic microHOs*. (**A**) A combined sample UMAP plot for the scRNA-seq data obtained from the cells in day 21 control (NC), PDGFB- (P) or TGFB (T)-treated microHO cultures. (**B**) The cell percentages for each of the 11 clusters in the different types of microHOs. (**C**) Boxplots show the changes in the percent of each indicated cell cluster in NC, PDGFB and TGFB treated microHOs. ns, not significant; *, p<0.05; or **, p<0.01. (**D**) RNA velocity results plotted on a UMAP plot. *Left*: stream embedding; *Middle*: velocity length indicates the rate of differentiation; *Right*: confidence, which is determined by the correlation of the velocity determined for neighboring clusters in the UMAP. *Bottom*: heatmap showing the velocity summary for all of the clusters. (**E**) Cell cycle phase is shown on the UMAP (Left); and the percentage of cells in each phase of the cell cycle is shown for NC, PDGFB- and TGFB-treated microHOs (Middle) or for all 11 clusters. (**F**) The Cytotrace score is plotted on the UMAP or as boxplots generated for the MyoF_T1, MyoF_P and Cho3 cells in NC, PDGFB- and TGFB-treated microHOs. (**G**) Among the cell types in human liver, the MyoF_T1 and MyoF_P transcriptomes are most similar to myofibroblasts, while Mes2 is most similar to HSC. These

34

violin plots show the results when the Mes2, MyoF_T1, and MyoF_P gene signatures were compared with the transcriptomes of the following cell types in normal and cirrhotic (GSE136103 (90)) human liver: VSMC, vascular smooth muscle; HSC, MyoF; and Meso, mesothelium. Each dot shows the module score of individual cells obtained for each of the four cell types. The MyoF_T1 and MyoF_P module scores are most similar to MyoF, and Mes2 has the most similarity with HSC in human liver. The MyoF module scores for MyoF_T1 and MyoF_P are 3-fold higher ($p<1\times10^{-10}$) than that of HSC, and the HSC gene signature module score for Mes2 is 4.8-fold ($p<1\times10^{-10}$) higher than for MyoF in human liver. (**H**) The bar graphs show the normalized enrichment score (NES) of the GSEA examining the association of the MyoF_T1 and MyoF_P gene signatures with liver tissue obtained from non-fibrotic (stage 1) or fibrotic (stage 4) NASH liver (GSE135251), and with resected hepatocarcinoma (HCC) tissue that was classified as non-fibrotic or fibrotic (GSE6764). The false discovery rate (FDR) p-value is indicated by the symbol above each bar: *, $P < 0.05$; **, $P<0.01$. The MyoF_T signature was strongly associated with fibrotic NASH liver; and both signatures were strongly associated with fibrotic HCC tissue but not with non-fibrotic NASH or HCC tissue. (**I**) Scatter plots that show the cell types that are the dominant senders (sources) and receivers (targets) of information, which regulate cellular interactions, as determined by CellChat analysis of scRNA-Seq data obtained from microHOs. The axes in the left and middle plots represent the total outgoing or incoming information associated with each indicated cell type. The dot size is proportional to the number of inferred links (both outgoing and incoming) for each cell type (indicated by dot color). The left plot shows the cell-cell communication networks based upon analysis of all signaling pathways in the CellChat database. The analyzed pathways include cytokines and chemokine pathways that promote cell growth and repair; extracellular matrix proteins that provide structural support and influence cell behavior; and adhesion molecules that direct cell-cell contact. The middle plot shows the cell-cell communication networks in the indicated cell types that were generated from CellChat analysis of only the "COLLAGEN pathway". *Right*: Illustration of the hypothesis generated by the Cellchat analysis. The highest level of inter-cellular communication occurs between MyoF_T1 and cholangiocytes.
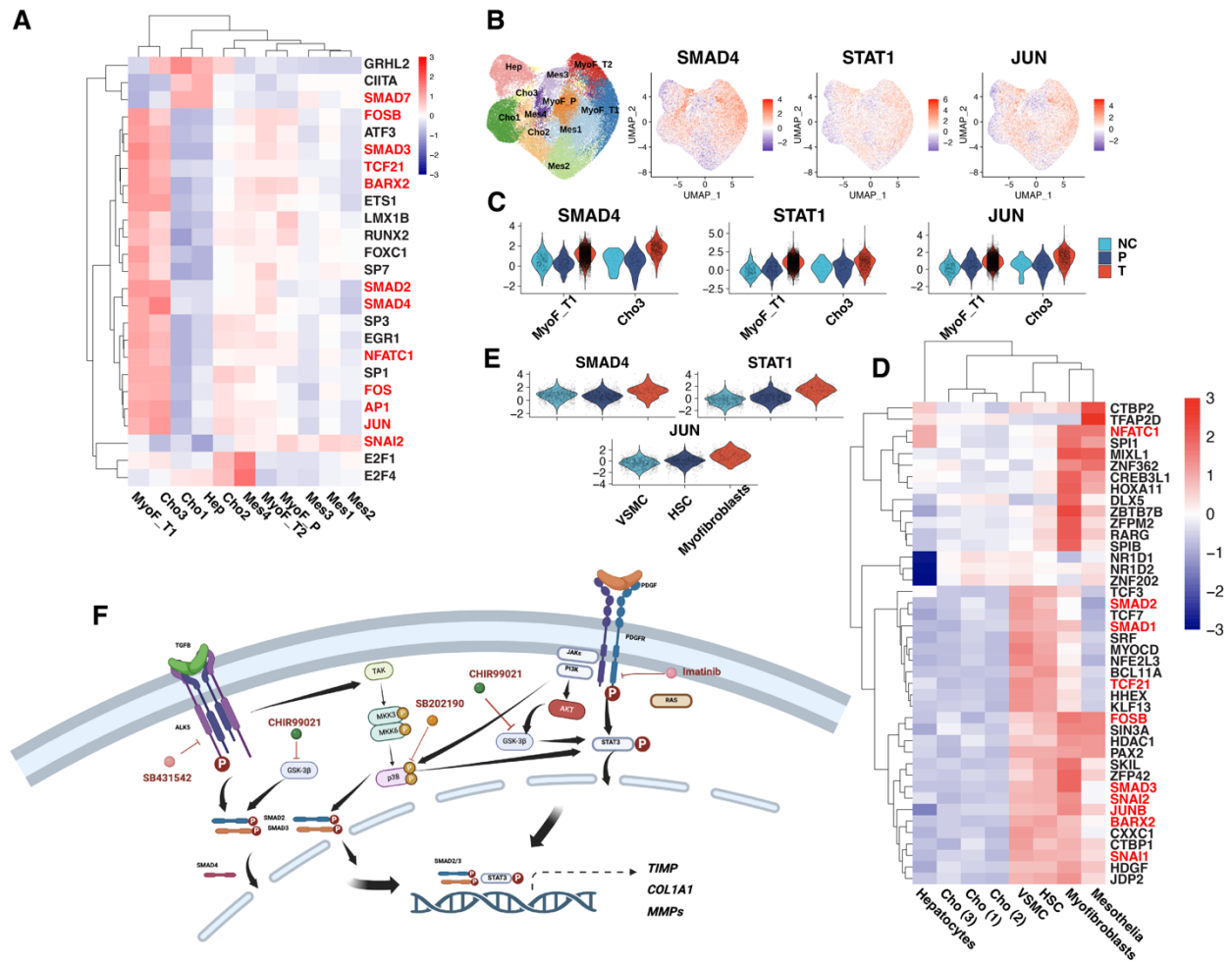
Figure 5. The transcription factors (TFs) activated in fibrotic microHOs and in fibrotic human liver. (**A**) A heat map shows the mean activity of the 25 TFs that were identified by decoupleR as being the ones that were most activated in fibrotic microHOs. The scaled mean activity for each TF in a cell cluster is indicated by the color of the square. Of note, MyoF_T1 and Cho3 had highest level of activation of these TFs. (**B**) SMAD4, STAT1 and JUN activity was plotted on the UMAP, and the cluster regions are indicated on the UMAP shown on the left. The scaled mean activity for each TF is indicated by dot color. The MyoF_T1 cluster had the highest level of activity of these TFs. (**C**) Violin plots show the TGFB-induced increased TF activity in the MyoF_T1 and Cho3 clusters. (**D**) A heat map shows the mean activity of the 42 TFs that were identified by decoupleR as being the ones that were most activated in fibrotic human liver. The scaled mean activity for each TF in a cell type is indicated by the color of the square. Myofibroblasts have the most activated TFs, and there is overlap with the TFs activated in MyoF1 in fibrotic microHOs (highlighted in red). (**E**) Violin plots show that myofibroblasts have an increased level of SMAD4, STAT1 and JUN activity versus that of vascular smooth muscle

cells or HSC. (**F**) Potential targets for anti-fibrotic drugs within the intracellular signaling pathways that are activated by TGFB or PDGFB. Pro-fibrotic agents activate the SMAD and STAT pathways, which can also activate the p38 MAPK and GSK3β pathways as shown in the diagram. Several potential targets for anti-fibrotic agents within SMAD, STAT and interacting (p38 MAPK and GSK3β) pathways are also indicated in the diagram.
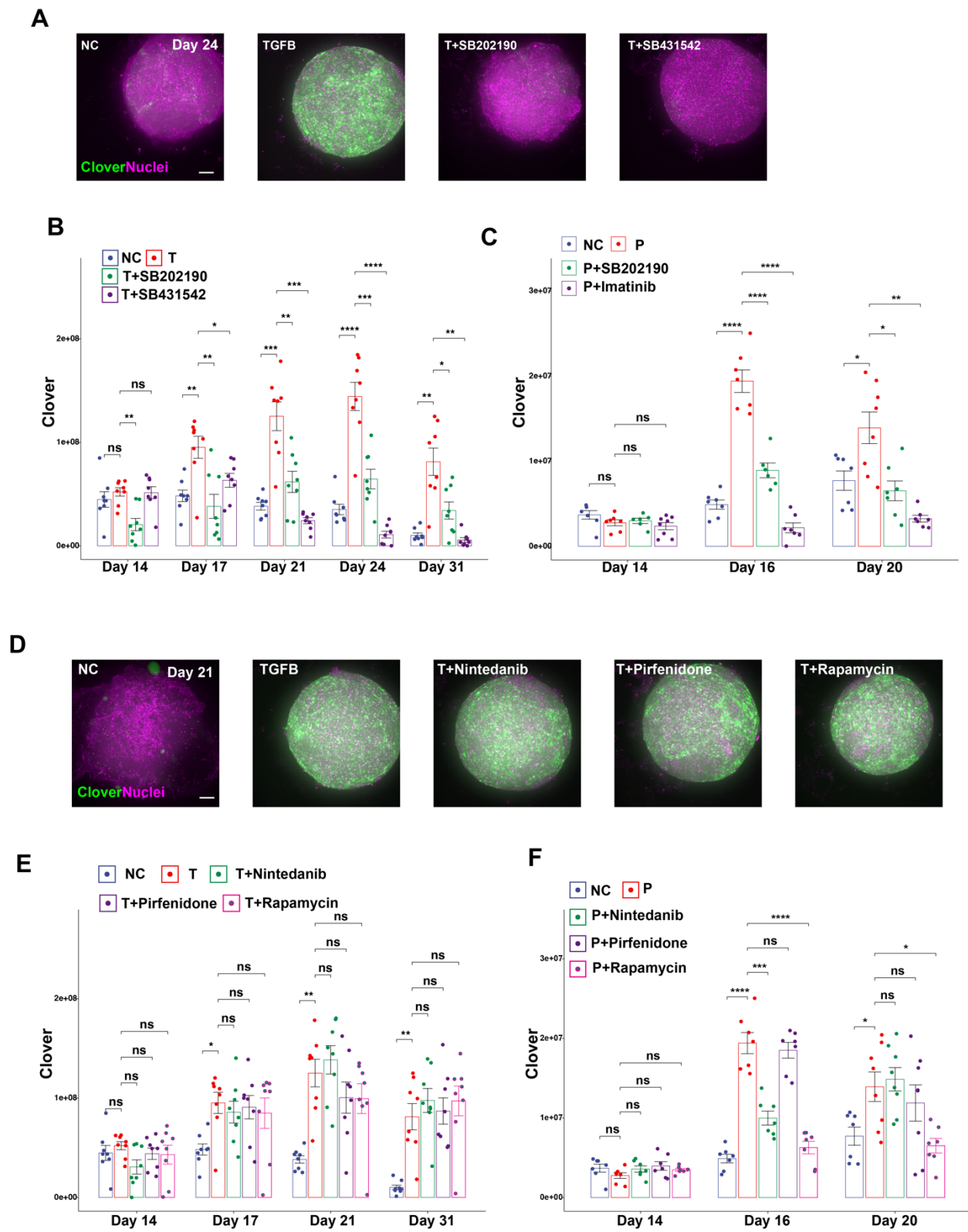
Figure 6. p38 MAPK inhibitor targets both TGFB and PDGFB pathway. (**A-C**) TGFB- or PDGFB-induced fibrosis in microHOs is inhibited by a p38 MAPK inhibitor. (**D-F**) PDGFB-

induced fibrosis is inhibited by pirfenidone or rapamycin. (**A**, **D**) Maximum intensity projection (MIP) images of z stack sections obtained from microHOs treated with no addition (NC), or 50 ng/ml TGFB$\pm$ 10 uM of the indicated drugs. Scale bar 100 um. Clover expression is green, and nuclei stained with Hoechst 33342 are purple. (**B-C**, **E-F**) The amount of COL1A1$^+$ cells within a microHO was serially measured on days 14 through 31. Each dot represents a measurement made on a microHO, the thick line is the median of 8 microHOs that were assessed, and the box plot shows the 25 to 75% range for all measurements per condition. When only growth factors were added, the p-values were relative to the NC, and the significance indicators are ns, not significant; *, $p<0.05$; **, $p<0.01$; ***, $p<0.001$ or ****, $p<0.0001$. When growth factors and inhibitors were added, the p-values were calculated relative to the PDGFB or TGFB treated microHOs (without added drug). A two-way ANOVA analysis indicates that drug treatment and time are two variables that have a significant interaction on the fluorescence measurements (Table S9).
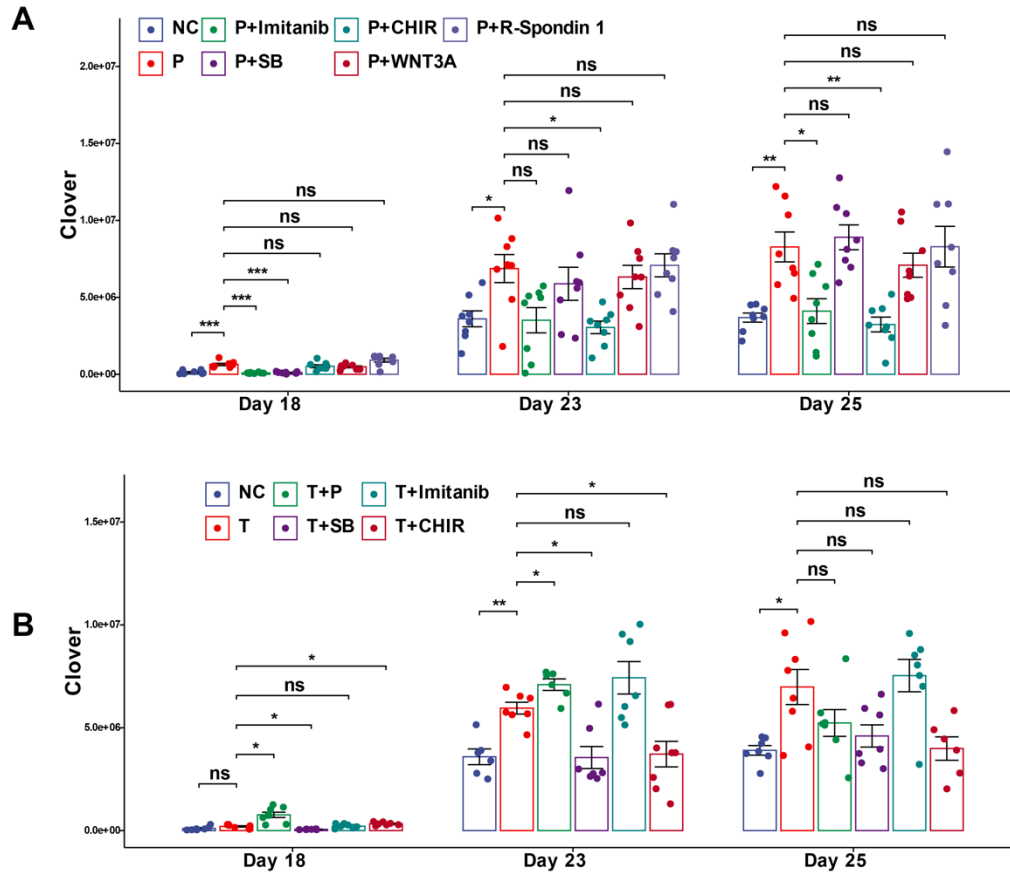
Figure 7. GSK3β inhibitors block TGFB and PDGFB-induced fibrosis. (**A**) The PDGFB-induced increase in COL1A1$^+$ cells is blocked by PDGFRβ and GSK3β inhibitors. *COL1A1*-P2A Clover HOs were formed by adding 10,000 cells from day 9 organoid cultures to each microwell. Then, either nothing (NC), 50 ng/ml PDGFB (P) or 50 ng/ml PDGFB with 10 μM imatinib, 10 uM SB431542 (SB), 10 uM CHIR99021 (CHIR), 100 ng/ml Wnt3a or 100 ng/ml R-spondin 1 was added to each microHO on day 13. **(B)** The TGFB induced increase in COL1A1$^+$ cells is blocked by TGFBR1 and GSK3β inhibitors. Either nothing (NC), 50 ng/ml TGFB (T), 50 ng/ml TGFB with 50 ng/ml PDGFB (T+P), or 50 ng/ml TGFB and either 10 μM imatinib, 10 uM SB431542 (SB), or 10 uM CHIR99021 (CHIR) was added to each microHO on day 13. microHO fluorescence, which indicates the amount of COL1A1$^+$ cells, was serially measured on days 18 through 25. Each dot represents a measurement made on a microHO, the thick line is the median for 8 microHOs that were assessed, and the box plot shows the 25 to 75% range for the measurements. In the panels: ns, not significant; *, p<0.05; or **, p<0.01, ***, p<0.001 for the measurement relative to the value in the NC; or when growth factors or inhibitors were added, the p-values were calculated relative to that of the PDGFB or TGFB treated cultures. A two-way

40

ANOVA indicates that drug treatment and time are two variables that have a significant interaction on the fluorescence measurements (Table S9).
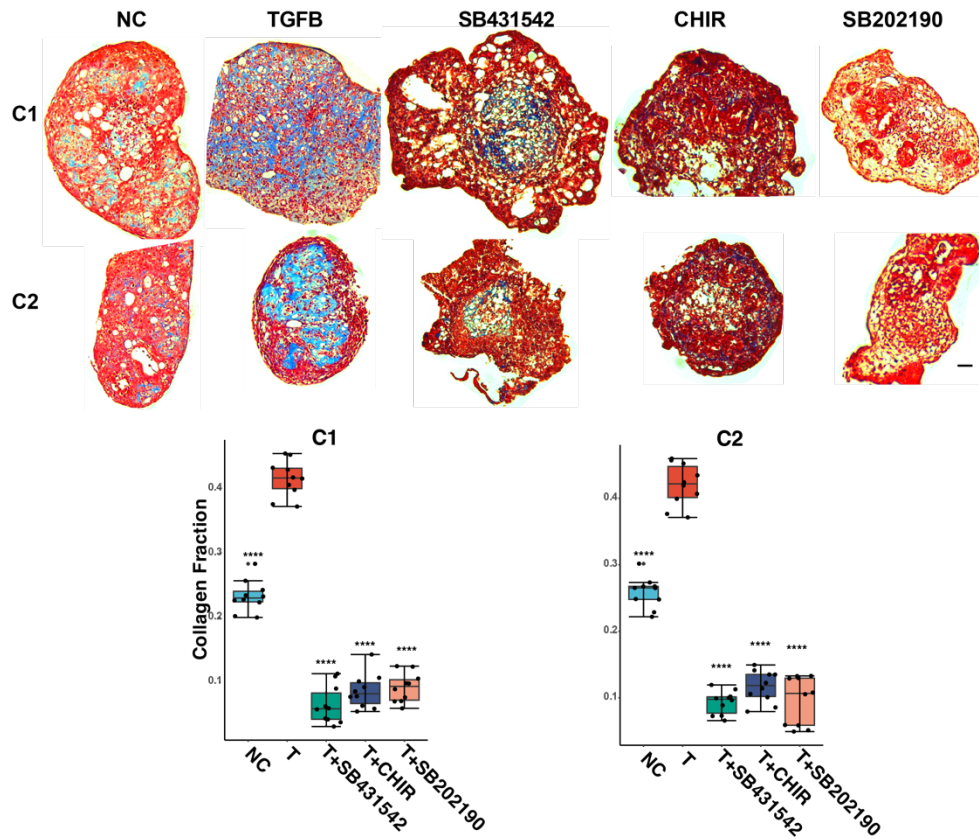
Figure 8. Anti-fibrotic drugs inhibit fibrosis in microHOs produced from iPSC of different genetic backgrounds. microHOs produced from iPSC lines generated from two donors (C1, C2) (10) were treated with no addition (NC), TGFB(T) (50 ng/ml), or TGFB and one of the following drugs on day 13: TGFBR inhibitor (10 μM SB431542), GSK3β inhibitor (3 μM CHIR) or a p38 inhibitor (10 μM SB202190). The microHOs were analyzed by trichrome staining on day 21. **(A)** Images of trichrome-stained TGFB-treated microHOs show a marked increase in collagen-rich connective tissue (blue stained regions) relative to control (NC) microHOs, which only had a thin layer of connective tissue. The TGFB-induced increased in collagen was markedly inhibited by addition of the TGFBR, GSK3β, or p38 inhibitors. The scale bar on the left: 50 μm. (**B**) Boxplots show the area in microHOs that received indicated treatments (n=6-9 per group) occupied by collagen (collagen fraction). The means for each group were compared using a one-way ANOVA and Tukey's post-test: ****, $p < 0.0001$ (for T vs NC, or T vs T+drug).